

THE MORPHOLOGY–DENSITY RELATION IN $Z \sim 1$ CLUSTERS

M. POSTMAN¹, M. FRANX², N.J.G. CROSS³, B. HOLDEN⁴, H.C. FORD³, G.D. ILLINGWORTH⁴, T. GOTO³, R. DEMARCO³, P. ROSATI⁵, J.P. BLAKESLEE³, K.-V. TRAN⁶, N. BENÍTEZ³, M. CLAMPIN⁷, G.F. HARTIG¹, N. HOMEIER³, D.R. ARDILA³, F. BARTKO⁸, R.J. BOUWENS⁴, L.D. BRADLEY³, T.J. BROADHURST⁹, R.A. BROWN¹, C.J. BURROWS¹⁰, E.S. CHENG¹¹, P.D. FELDMAN³, D.A. GOLIMOWSKI³, C. GRONWALL¹², L. INFANTE¹³, R.A. KIMBLE⁷, J.E. KRIST¹, M.P. LESSER¹⁴, A.R. MARTEL³, S. MEI³, F. MENANTEAU³, G.R. MEURER³, G.K. MILEY², V. MOTTA¹³, M. SIRIANNI¹, W.B. SPARKS¹, H.D. TRAN¹⁵, Z.I. TSVETANOV³, R.L. WHITE¹ & W. ZHENG³

Accepted for publication in the Astrophysical Journal

ABSTRACT

We measure the morphology–density relation (MDR) and morphology–radius relation (MRR) for galaxies in seven $z \sim 1$ clusters that have been observed with the Advanced Camera for Surveys on board the Hubble Space Telescope. Simulations and independent comparisons of our visually derived morphologies indicate that ACS allows one to distinguish between E, S0, and spiral morphologies down to $z_{850} = 24$, corresponding to $L/L^* = 0.21$ and 0.30 at $z = 0.83$ and $z = 1.24$, respectively. We adopt density and radius estimation methods that match those used at lower redshift in order to study the evolution of the MDR and MRR. We detect a change in the MDR between $0.8 < z < 1.2$ and that observed at $z \sim 0$, consistent with recent work – specifically, the growth in the bulge-dominated galaxy fraction, f_{E+S0} , with increasing density proceeds less rapidly at $z \sim 1$ than it does at $z \sim 0$. At $z \sim 1$ and $\Sigma \geq 500$ galaxies Mpc^{-2} , we find $\langle f_{E+S0} \rangle = 0.72 \pm 0.10$. At $z \sim 0$, an E+S0 population fraction of this magnitude occurs at densities about 5 times smaller. The evolution in the MDR is confined to densities $\Sigma \gtrsim 40$ galaxies Mpc^{-2} and appears to be primarily due to a deficit of S0 galaxies and an excess of Spiral+Irr galaxies relative to the local galaxy population. The f_E – density relation exhibits no significant evolution between $z = 1$ and $z = 0$. We find mild evidence to suggest that the MDR is dependent on the bolometric X-ray luminosity of the intracluster medium. Implications for the evolution of the disk galaxy population in dense regions are discussed in the context of these observations.

Subject headings: galaxies: clusters: general — galaxies: formation — galaxies: evolution — galaxies: structure

1. INTRODUCTION

The study of the origin and evolution of the morphological distribution of galaxies in different environments can reveal important information about internal galactic stellar and gas dynamics, the state of star formation ac-

tivity as a function of time, and constrain the relative significance of the effects of environmental processes versus conditions at the epoch of their formation in establishing galactic structure. In standard hierarchical clustering models, galaxies in high density regions of the Universe, such as in the central regions of galaxy clusters, will collapse earlier and may evolve more rapidly than galaxies in low density regions (Kauffmann 1995; Benson et al. 2001, Heavens et al. 2004). In addition, galaxies in dense environments are subject to a variety of external stresses, which are, in general, not conducive to the maintenance of spiral structure. These processes include ram-pressure stripping of gas (Gunn & Gott 1972; Farouki & Shapiro 1980; Kent 1981; Fujita & Nagashima 1999; Abadi, Moore & Bower 1999; Quilis, Moore & Bower 2000), galaxy harassment via high speed impulsive encounters (Moore et al. 1996, 1999; Fujita 1998), cluster tidal forces (Byrd & Valtonen 1990; Valluri 1993; Fujita 1998) which distort galaxies as they come close to the center, interaction/merging (Icke 1985; Lavery & Henry 1988, Mamon 1992; Makino & Hut 1997; Bekki 1998), and removal and consumption of the gas due to the cluster environment (Larson, Tinsley & Caldwell 1980; Bekki et al. 2002).

Two of key relationships that must be understood in the context of the above processes are the relative population fraction of the different morphological classes as functions of the local galaxy density and their location within the local gravitational potential well. The morphology – density relation (hereafter MDR) and

¹ Space Telescope Science Institute, 3700 San Martin Drive, Baltimore, MD 21218.

² Leiden Observatory, Postbus 9513, 2300 RA Leiden, Netherlands.

³ Department of Physics and Astronomy, Johns Hopkins University, 3400 N. Charles Street, Baltimore, MD 21218.

⁴ UCO/Lick Observatory, University of California, Santa Cruz, CA 95064.

⁵ European Southern Observatory, Karl-Schwarzschild-Strasse 2, D-85748 Garching, Germany.

⁶ Institute for Astronomy, ETH Zürich, Scheuchzerstrasse 7, CH-8093 Zurich, Switzerland.

⁷ NASA Goddard Space Flight Center, Code 681, Greenbelt, MD 20771.

⁸ Bartko Science & Technology, 14520 Akron Street, Brighton, CO 80602.

⁹ Racah Institute of Physics, The Hebrew University, Jerusalem, Israel 91904.

¹⁰ MetaJiva Scientific.

¹¹ Conceptual Analytics, LLC, 8209 Woburn Abbey Road, Glenn Dale, MD 20769

¹² Department of Astronomy and Astrophysics, The Pennsylvania State University, 525 Davey Lab, University Park, PA 16802.

¹³ Departamento de Astronomía y Astrofísica, Pontificia Universidad Católica de Chile, Casilla 306, Santiago 22, Chile.

¹⁴ Steward Observatory, University of Arizona, Tucson, AZ 85721.

¹⁵ W. M. Keck Observatory, 65-1120 Mamalahoa Hwy., Kamuela, HI 96743

the morphology – radius relation (hereafter MRR) have been well studied at low- z (Dressler 1980 - hereafter D80; Postman & Geller 1984 - hereafter PG84; Whitmore & Gilmore 1991; Goto et al. 2003a) and quantify many long-standing observations showing a preference for spheroidal systems to reside in dense regions (or perhaps better stated as a significant lack of spiral galaxies in dense regions). A full understanding of how such a cosmic arrangement came to be requires measuring the evolution of the MDR and MRR. Such an evolutionary study is only possible using the high angular resolution provided by the Hubble Space Telescope (HST). Several pioneering works have now shed light on this evolution (Dressler et al. 1997 – hereafter D97; Fasano et al. 2000; Treu et al. 2003; Smith et al. 2004 – hereafter Sm04). D97 and Fasano et al. (2000) find a significant decline in the fraction of lenticular galaxies (f_{S0}) when one looks back from the present epoch to an epoch 4 – 5 Gyr ago. The results presented by Treu et al. 2003 and Sm04 are perhaps the most enlightening - they find a smaller increase in the bulge-dominated galaxy (E+S0) fraction (f_{E+S0}) with increasing density at $z \gtrsim 0.4$ than is seen at $z < 0.1$ but also find comparable f_{E+S0} values for low-density regions ($\Sigma < 10$ galaxies Mpc^{-2}) at $z \gtrsim 0.4$ and the current epoch. Sm04 propose a simple model to explain these observations in which high density regions at $z \sim 1$ would largely be comprised of elliptical galaxies with only a trace of lenticulars (*e.g.*, $0 \leq f_{S0} < 0.1$). They consider various processes to transform spiral galaxies into lenticular galaxies in order to increase f_{S0} with time to match the observed morphological population fractions at $z \sim 0.5$. However, the Sm04 $z \sim 1$ f_{S0} measurement was inferred from f_{E+S0} rather than measured directly as Sm04 chose (perhaps wisely) not to attempt to distinguish between S0 and E galaxies from the WFPC2 data used in their study.

The deployment of the Advanced Camera for Surveys (ACS; Ford et al. 2003) on the HST has provided us with an opportunity to greatly expand our understanding of the physics behind the morphological evolution of galaxies in a wide variety of environments. The higher sensitivity and better angular sampling of the Wide Field Camera (WFC) on ACS relative to WFPC2 enables the acquisition of high S/N morphological information for sub- L^* galaxies over projected areas of up to 10 Mpc^2 in $z \sim 1$ clusters, in a modest allocation of telescope time. This is a significant advantage over prior capabilities and enables us to sample > 3 decades in local galaxy density using the same homogeneous data samples.

As part of an extensive program to study the formation and evolution of clusters and their galaxy populations, the ACS Investigation Definition Team (IDT) has implemented a 128 orbit program to observe 7 distant clusters in the redshift range $0.83 \leq z \leq 1.27$. In this paper, we present new constraints on the form and evolution of both the MDR and the MRR in these clusters and their surroundings based on morphologies determined from the ACS/WFC imagery coupled with extensive spectroscopic data and X-ray observations. This paper is organized as follows: section 2 contains a brief summary of the space and ground-based observations used in this study, section 3 presents a detailed discussion of our morphological classification procedure and an assessment of the reliability of these classifications, section 4 presents the methods

used to estimate the local projected density, and section 5 presents our derived MDR and MRR. An assessment of the implications of these results is given in section 6 and a summary of the essential results is provided in section 7. Two appendices discuss details associated with the computation population fractions that are suitably corrected for contamination and incompleteness, the robustness of our density estimators, and the validity of using composite samples to enhance the signal-to-noise ratio in the derived MDR and MRR. We adopt $H_o = 70 \text{ km s}^{-1} \text{ Mpc}^{-1}$, $\Omega_m = 0.3$, and $\Omega_\Lambda = 0.7$ for the computation of all intrinsic quantities unless specifically indicated otherwise.

2. OBSERVATIONS

The clusters included in this study, along with a summary of the ACS observations, are listed in Table 1. The average cluster redshift, based on all available spectroscopically confirmed cluster members, is given in column 2 of this table. The number of redshifts acquired for galaxies in the region of each cluster (both members and non-members and including galaxies outside the ACS mosaic boundaries) is listed in column 3. Column 4 lists the number of spectroscopically confirmed cluster members that also lie within the ACS mosaic boundaries. The details of the HST ACS observations are given in columns 5 – 7. The sample selection process was limited by the small number of spectroscopically confirmed clusters at $z > 0.8$. However, we were able to include clusters with a range of X-ray luminosities, from $L_{x,\text{Bol}} < 10^{44} \text{ erg s}^{-1}$ to $L_{x,\text{Bol}} = 1.9 \times 10^{45} \text{ erg s}^{-1}$. Table 2 is a compilation of the derived X-ray properties and velocity dispersions of these clusters. Two of the seven clusters (the two at R.A. = 16 hr) are optically selected systems, the rest are X-ray selected although RXJ0849+4452 is a binary cluster system in which the less massive component (CL J0848+4453) was IR-selected (Stanford et al. 1997).

2.1. ACS Observations

We used the WFC on the ACS to image each cluster. For MS1054-0321, RXJ0152-1357, RDCS1252-2927, and RXJ0849+4452 multiple pointings were used to construct larger mosaics covering ~ 35 square arcminutes. For the first three of these clusters, the pointings form a 2×2 pattern with all 4 pointings overlapping the central 1 arcminute region of each cluster - hence the exposure time in the central regions of these systems is 4 times as long as the values given in Table 1. For RXJ0849+4452, we used a 3×1 pattern in order to obtain images of both components of this binary cluster system. All the remaining targets were observed using a single WFC pointing centered on the cluster.

The filters are chosen to approximately straddle the rest-frame 4000\AA break in order to facilitate the identification of bulge-dominated galaxies in the red sequence of the clusters. This sequence, which is populated mostly by elliptical and lenticular galaxies with a strong 4000\AA break, is well separated from the CM relation for late-type cluster galaxies as well as that for most field galaxies. In all cases, we have at least one filter that samples part of the rest-frame B -band. We use the ACS images taken in those filters to perform our morphological classifications so that we can readily compare our results with morphological information obtained at lower

redshifts (e.g., Fabricant, Franx, & van Dokkum 2000). The filters used are explicitly listed in Table 1. Hereafter, we will use V_{606} to denote the F606W bandpass, r_{625} to denote F625W, i_{775} to denote F775W, I_{814} to denote F814W, and z_{850} to denote F850LP.

2.2. Object Photometry and Classification

Object detection and analysis is performed using the ACS IDT Pipeline (*a.k.a.* APSIS; Blakeslee et al. 2003a). APSIS photometry is on the AB system and is corrected for Galactic extinction using the Schlegel et al. (1998) 100μ map. Object detection and star-galaxy discrimination is done using the dual image mode in SExtractor (Bertin & Arnouts 1996). The detection image is an inverse variance weighted combination of the ACS exposures from all available passbands. The inverse variance weighting preserves information about the structural characteristics of the galaxies (see Benítez et al. 2004 for details). In this paper, we count as galaxies all objects with SExtractor stellerity parameter CLASS_STAR ≤ 0.50 . The automated image structure analysis of detected objects in our ACS data includes the determination of the luminosity-weighted moments, the ellipticity, and the 180° rotational asymmetry and image concentration parameters (*e.g.*, Abraham et al. 1994; Conselice et al. 2000). All magnitudes cited in this study are based on the SExtractor MAG_AUTO magnitude as it provides a reasonable estimate of the total flux.

2.3. Spectroscopic Observations and Photometric Redshifts

Spectroscopic redshifts have been obtained for the clusters in our survey, by us and others, using multiobject spectrographs on the Keck, VLT, or the Magellan observatories. The total number of redshifts and the number of confirmed cluster members within each ACS mosaic are listed in Table 1. The publications containing some or all of the redshift data include Tran et al. (2005) for MS1054-0321, Demarco et al. (2004) for RXJ0152-1357, Postman et al. (1998a, 2001) and Gal & Lubin (2004) for the CL1604+43 system, Stanford et al. (2002) for RDCS0910+5422, Demarco et al. (2005) for RDCS1252-2927, and Rosati et al. (1999) for RXJ0849+4452. The target selection criteria for the redshift surveys of MS1054-0321 and the CL1604+43 clusters were based on a single red flux limit. The target selection for RXJ0152-1357 include a color-selection criterion (see Demarco et al. 2004). The spectra are of moderate resolution ($R \sim 500 - 1200$) and most have sufficient S/N to measure the prominent spectral features (*e.g.*, [OII] line widths).

Our photometric redshifts are derived using the Bayesian method (*a.k.a.* BPZ) described in Benítez (2000) and are based on a minimum of 3 passbands, including all available ACS photometry. We have reliable photo- z 's for RXJ0152-1357 ($z = 0.837$), MS1054-0321 ($z = 0.831$), and RDCS1252-2927 ($z = 1.235$). Photo- z 's for RXJ0152-1357 are based on the ACS r_{625} , i_{775} , and z_{850} photometry. Photo- z 's for MS1054-0321 are based on the ACS V_{606} , i_{775} , and z_{850} photometry. Photo- z 's for RDCS1252-2927 are based on ACS i_{775} , z_{850} photometry and ground-based $BVJK$ photometry (Toft et al. 2004). For the two $z = 0.83$ clusters, the rms scatter

in $(z_{spec} - z_{ph})/(1 + z_{spec})$, σ_{ph} , is 0.05. For RDCS1252-2927, σ_{ph} is 0.10. Only objects that have a BPZ confidence level of 0.90 or greater are selected for analysis. Figure 1 shows the distribution of galaxies with photometric redshifts within $2\sigma_{ph}$ of the mean cluster redshift and galaxies with $2\sigma_{ph} < |\bar{z}_{CL} - z_{ph}|/(1 + z_{CL}) < 6\sigma_{ph}$. The cluster overdensity is clearly seen only when we select galaxies close to the actual mean cluster redshift, indicating our photo- z 's are useful in significantly suppressing fore/background contamination and isolating most of the actual cluster members.

3. MORPHOLOGICAL CLASSIFICATION

We visually classified the morphologies of all galaxies in each field with $i_{775} \leq 23.5$ (for the $z < 1$ clusters) or $z_{850} \leq 24$ (for the $z > 1$ clusters) regardless of their position or color. For reference, the characteristic magnitude, m^* , for cluster galaxies is $i_{775} = 22.3$ at $z = 0.83$ (Goto et al. 2004) and $z_{850} = 22.7$ at $z = 1.24$ (Blakeslee et al. 2003b). For all our cluster observations, we have at least one filter that samples part of the rest-frame B -band (see Table 1) so that morphological classifications can be readily compared with those at lower redshifts. We classify galaxies using the common Hubble sequence: E, E/S0, S0, S0/Sa, Sa, Sb, Sb/Sc, Sc/Sd, Irr. However, for the purposes of the present analyses, we bin these finer classifications into just 3 broad morphological categories: E (elliptical; $-5 \leq T \leq -3$), S0 (lenticular; $-2 \leq T \leq 0$), and Sp+Irr (Spiral + Irregular; $1 \leq T \leq 10$). The FWHM of the point spread function in our co-added ACS images is ~ 0.09 arcsec (1.8 WFC pixels), corresponding to a projected proper distance of 684 pc at $z = 0.831$ and 752 pc at $z = 1.27$. We are thus able to resolve sub-kpc structure in all cluster members. At $i_{775} = 23.5$, the typical galaxy subtends an isophotal area of ~ 400 WFC pixels or $125 \times (\text{FWHM})^2$, making visual classification (or for that matter any classification method) quite feasible. At fainter magnitudes, however, classification rapidly becomes difficult and systematic errors increase both because galaxies are becoming smaller (*e.g.*, Roche et al. 1998; Bouwens et al. 1998; Ferguson et al. 2004; Trujillo et al. 2004) and because there is insufficient area over which the integrated S/N is sufficient for accurate classification. Examples of the ACS image quality and our corresponding classifications are shown in Figures 2 and 3.

The morphological classification was performed on the full sample of 4750 galaxies (in 7 clusters) by one of us (MP). Three other team members (NC, MF, BH) classified a subset of ~ 400 of these galaxies to provide an estimate of the uncertainty in the classifications. All classifiers used a common reference set of morphologies from a low redshift B -band galaxy sample as a guide. Exact or majority agreement between all 4 classifiers in the overlap sample was typically achieved for 75% of the objects brighter than $i_{775} = 23.5$. Furthermore, there was no significant systematic offset between the mean classification for the 3 independent classifiers (as determined using the voting scheme from Fabricant et al. 2000) and the classification by MP giving confidence that the full sample was classified in a consistent manner.

The overall population fractions between the 4 independent classifiers exhibit only a relatively small variance. Figure 4 shows the E+S0 fraction for each classi-

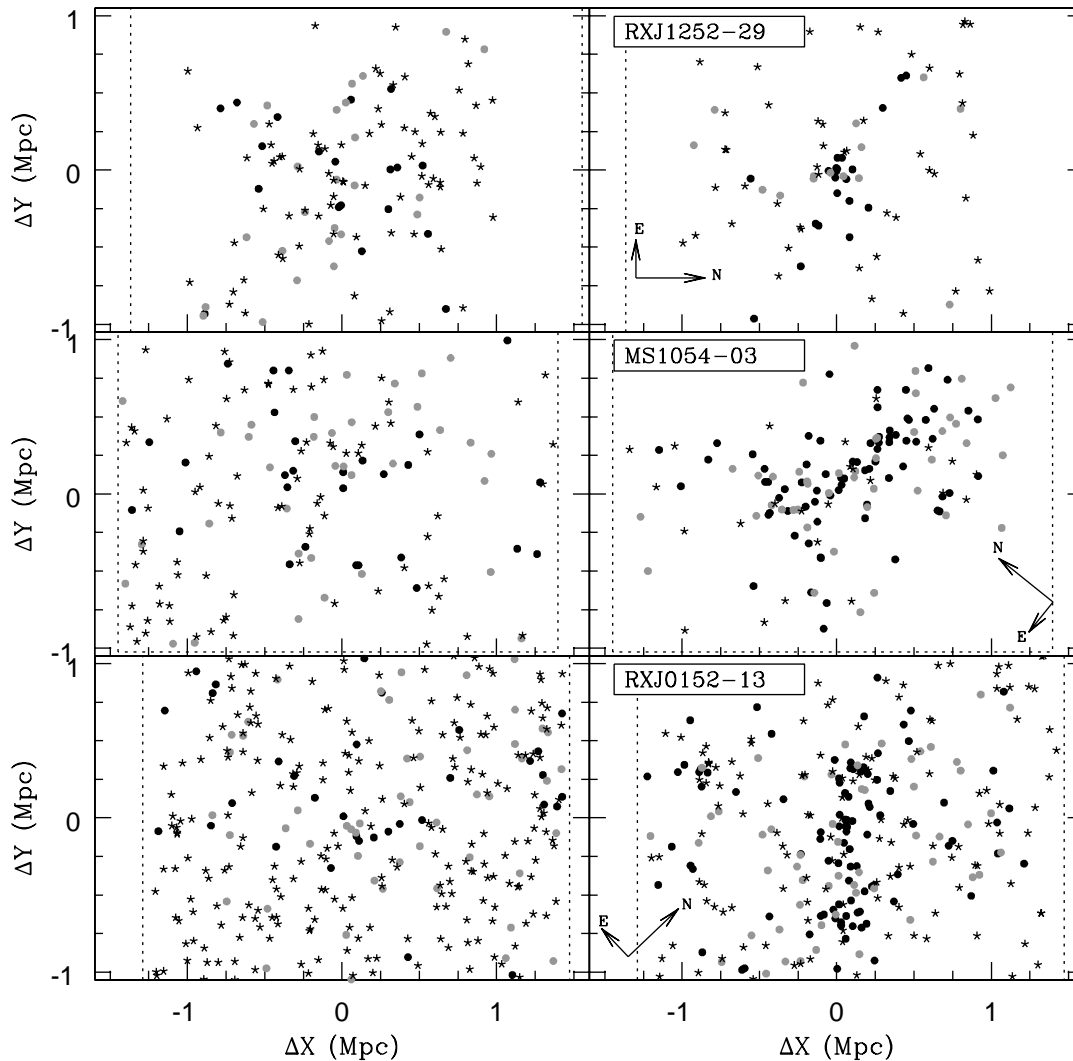


FIG. 1.— The projected distribution of galaxies with photometric redshifts that lie within $\pm 2\sigma_{ph}$ of the mean cluster redshift are shown in the right-hand panels for RXJ0152-1357, MS1054-0321, and RDCS1252-2927. The distribution of galaxies with photometric redshifts in the range $2\sigma_{ph} < |\bar{z}_{CL} - z_{ph}| / (1 + z_{CL}) < 6\sigma_{ph}$ are shown in the left-hand panels. Different symbols denote different morphological classifications: black dots are ellipticals, grey dots are S0's, and stars are Sp+Irr. The dashed lines denote the boundaries of the ACS mosaics. The RDCS1252-2927 photo- z 's are available over less area than the full ACS mosaic because they rely on NIR photometry that covers a smaller region. The overdensities associated with the clusters are easily seen in the right-hand panels and are dominated by E and S0 galaxies.

fier as a function of z_{850} magnitude for a color-selected ($i_{775} - z_{850} \geq 0.5$) subset of galaxies in the RDCS1252-2927 field. The average rms scatter in the E+S0 population fraction between classifiers is 0.06. The average rms scatter in the S0 population fraction between classifiers is about 2 times higher, 0.11. The rms in the E population fraction is the same as that for the S0's, 0.11. In other words, the population fractions are fairly robust and the variance in these fractions is significantly less than the $\sim 20 - 25\%$ disagreement level between classifiers on the morphological classification of any individual galaxy. Not surprisingly, the combined E+S0 fraction is more robust than either the E or the S0 fractions – a quantitative demonstration that detecting spiral structure is a more robust skill than detecting disks. Most im-

portantly, there are no significant systematic differences between the classifiers. The scatter in the S0 population fraction is comparable with \sqrt{N} uncertainties in any given value and while counting statistics do not suggest the minimum scatter one might expect between different classifiers, this level of scatter indicates that our classification errors are small enough for the task at hand – providing a uniform set of classifications.

If our visual morphological classifications are robust, there should be noticeable differences in the distributions of the objectively derived “form” parameters (ellipticity, asymmetry, concentration) for the E, S0, and Sp+Irr categories. Figure 5 shows the histograms of these 3 form parameters for each of the 3 morphological bins. Clear differences between the distributions exist. For example,

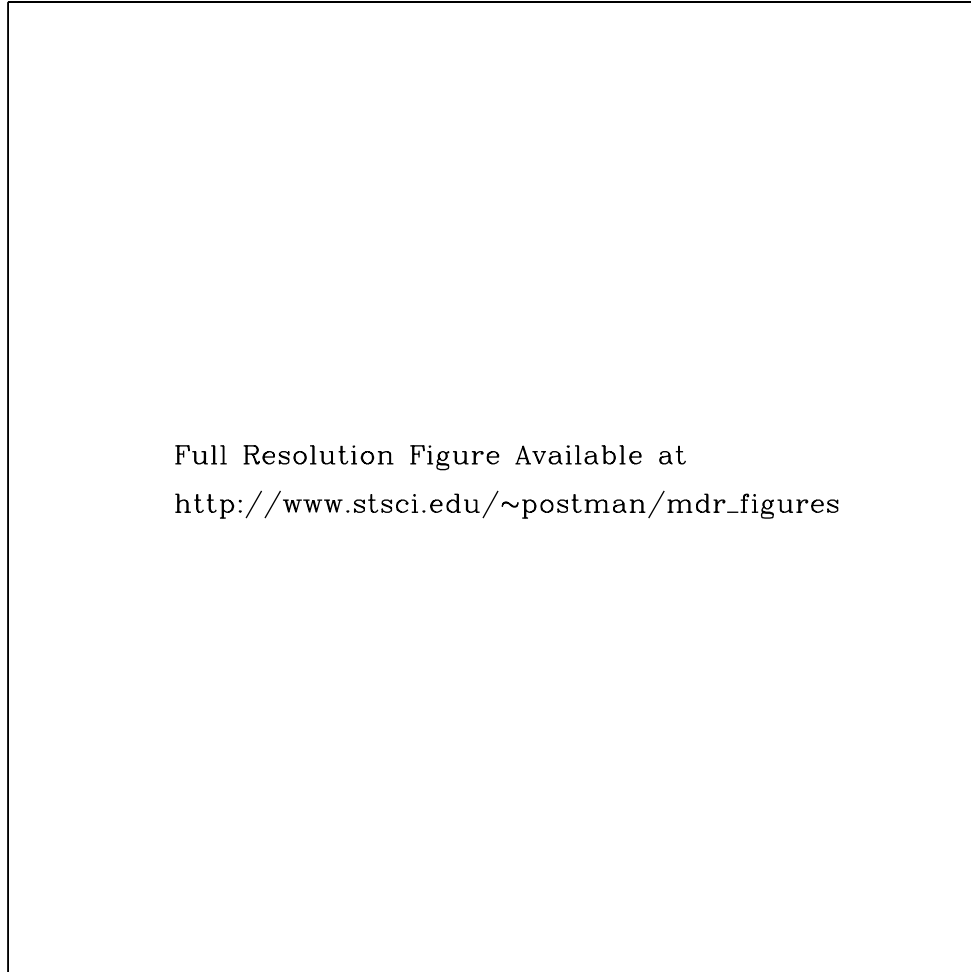
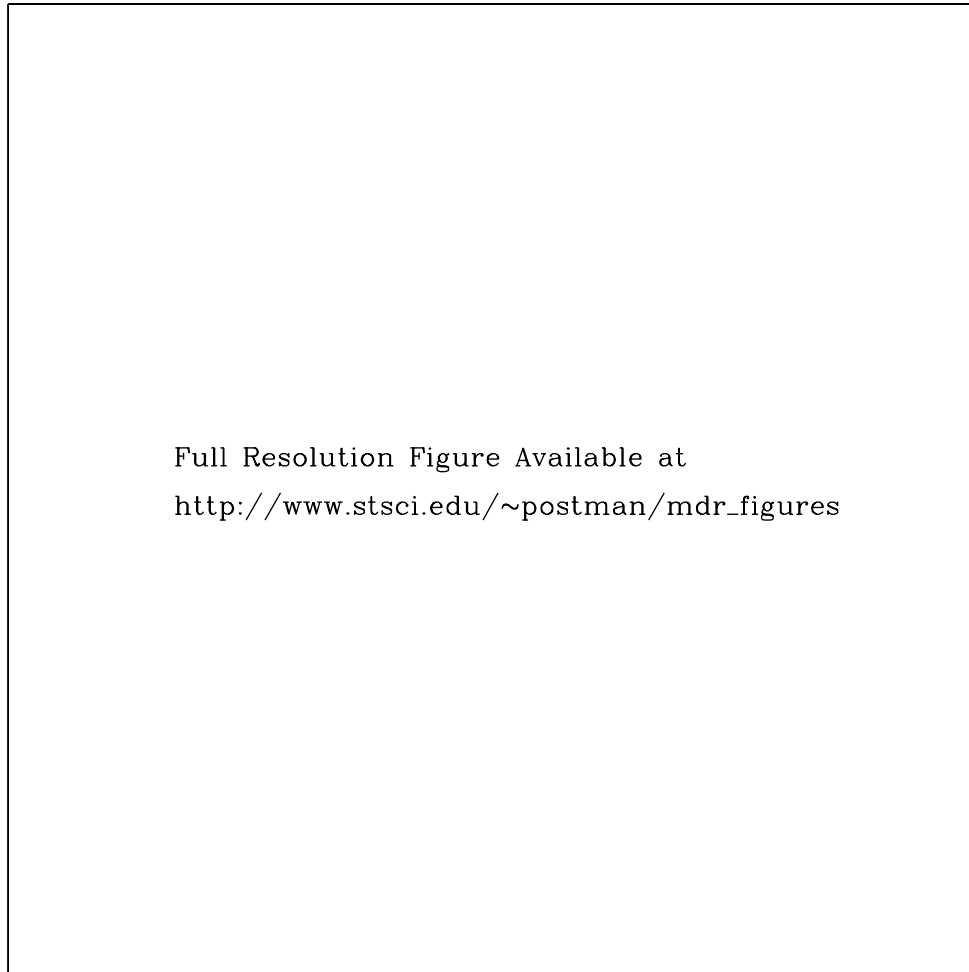


FIG. 2.— Color postage stamp cutouts of the brightest 49 spectroscopically confirmed members of CL1604+4321 ($z = 0.92$) and CL1604+4304 ($z = 0.90$) and their corresponding visually derived morphological classifications. The “Pos Disk” classification stands for “possible disk” galaxy. It is given to objects that appear to have a disk structure but the precise nature of that disk could not be established. Galaxies with the “Pos Disk” classification are counted as Spirals in our derivation of the MDR. The first 29 cells show galaxies from CL1604+4321 and the rest contain galaxies from CL1604+4304. The galaxies from each cluster are shown in increasing apparent magnitude order and span the range $20.91 \leq i_{775} \leq 23.50$. Each cutout subtends a 6.4×6.4 arcsecond area.

the ellipticity distribution of visually classified elliptical galaxies differs from that for visually classified S0 galaxies at greater than the 99.999% confidence level. We will use this fact later on as a key part of our analysis. Ellipticals as a class have, as expected, a lower median ellipticity and asymmetry and a higher median concentration than the other two morphological classes. Ellipticals also exhibit less scatter about the mean values of these form parameters. The Sp+Irr class exhibits a higher mean ellipticity and asymmetry than either the E or S0 class. The S0 galaxies have form characteristics that are, on average, intermediate between the E and Sp+Irr distributions.

Two key concerns when performing galaxy morphological classification, visually or via machine algorithms, are the effect of surface brightness dimming and the

shorter rest-frame wavelength being imaged with increasing redshift. The latter effect, sometimes referred to as the “morphological k-correction,” has been studied fairly well (Bunker et al. 2000, Abraham & van den Bergh 2001, Windhorst et al. 2002, Papovich et al. 2003). In general, over the redshift range being studied here, the morphological k-correction has been shown to be important only in a small fraction ($\lesssim 20\%$) of the galaxy population and in those cases, it is often more of an issue of how one characterizes any existing spiral structure and not usually a case of missing spiral structure altogether (see references above for details). Furthermore, the bluest wavelengths we use for our morphological classifications correspond to the blue end of the rest-frame B -band, which is where many lower redshift studies have been done. Our classi-



Full Resolution Figure Available at
http://www.stsci.edu/~postman/mdr_figures

FIG. 3.— Color postage stamp cutouts of the brightest 49 spectroscopically confirmed members of MS1054-0321 ($z = 0.831$). The galaxies are displayed in increasing apparent magnitude order and span the range $20.14 \leq i_{775} \leq 22.15$.

fications are never performed in the rest-frame U -band.

The effects of SB dimming are potentially of greater concern as the ability to distinguish between adjacent categories (*e.g.*, E vs S0, S0 vs Sa) may be compromised at higher redshift. To test how sensitive our visual classification scheme is to SB-dimming, we performed two simulations. In the first test, we “redshift” our ACS image of the $z = 0.33$ cluster MS1358+6245 to $z = 0.83$ and perform visual classifications on both the original and redshifted versions. In the second test, we redshifted our ACS image of MS1054-0321 to $z = 1.24$ and compared the classifications derived for the original and redshifted versions. The “redshifting” involved dimming the objects appropriately, resampling the images to account for the smaller angular scale, and adjusting the noise levels to correspond to those appropriate for our exposure times used in the more distant cluster observations. Re-classification of the redshifted galaxy images was done in a random order and at least 3 months after the initial

classifications to minimize “memory” of the initial classifications by the classifier. Some examples of the original and redshifted MS1054-0321 galaxies are shown in Figure 6. The results of the comparisons between the morphological classifications of the original and redshifted objects are shown in Figure 7. The population fractions obtained using the redshifted images are completely consistent with those in the original images – the differences are comparable to or less than the \sqrt{N} uncertainties. Thus, our increased exposure times for the more distant clusters coupled with the high angular sampling and sensitivity of the ACS/WFC successfully mitigate the effects of SB-dimming and allow us to distinguish between our 3 primary morphological categories (E, S0, and Sp+Irr) uniformly across the redshift range under study.

3.1. Classification of Mergers & External Morphology Comparisons

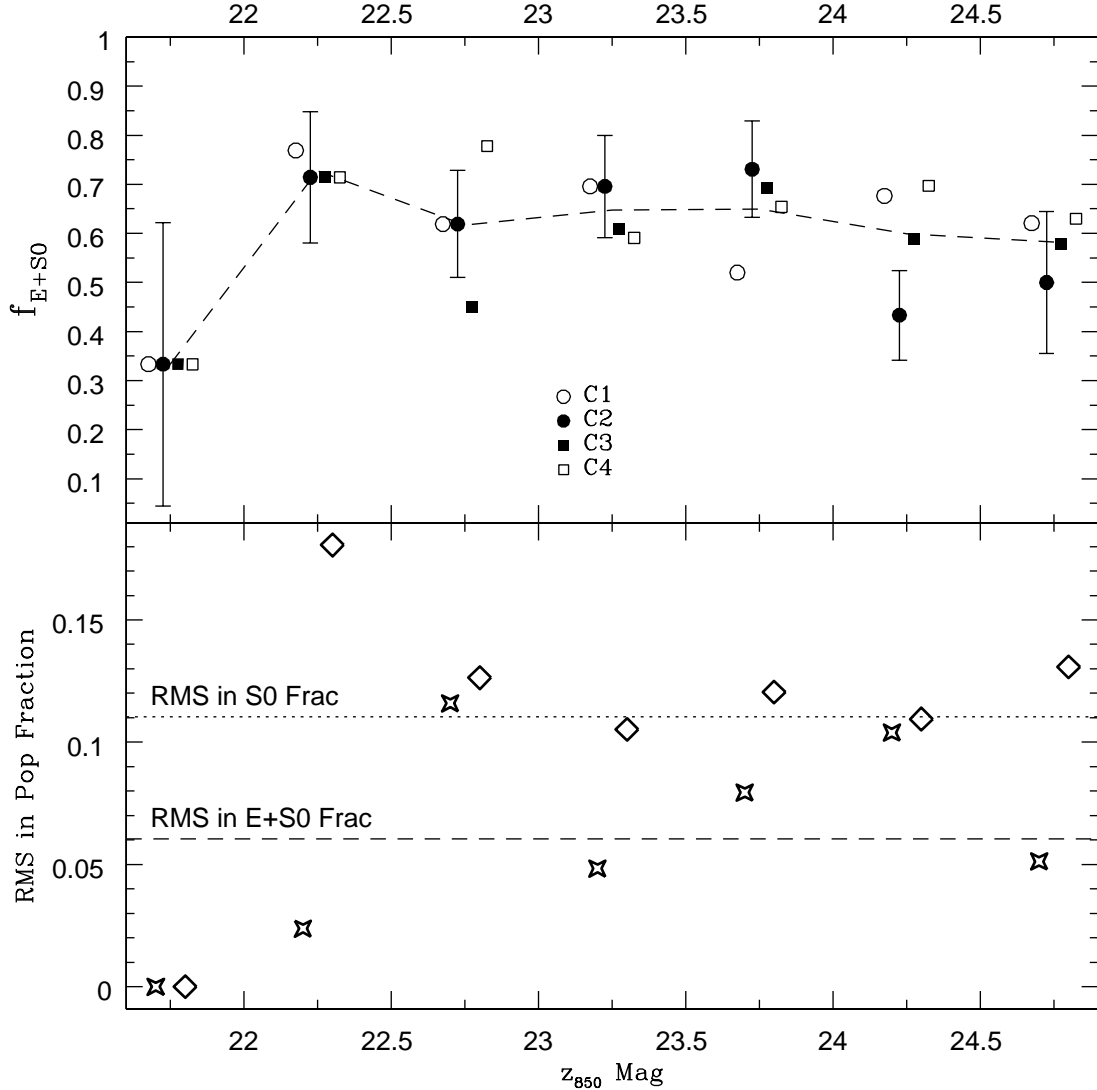


FIG. 4.— **Upper panel:** The E+S0 population fraction as a function of z_{850} magnitude for each of the 4 independent visual classifiers. The sample used in this comparison is a color-selected sample that favors inclusion of bulge-dominated galaxies, hence the relatively high overall early-type population fraction. The values for each classifier are offset slightly from one another for clarity. The error bars shown represent the \sqrt{N} uncertainties. The dashed line shows the mean E+S0 population fraction averaged over all classifiers. **Lower panel:** The RMS scatter in the E+S0 (stars) and S0 (diamonds) population fractions as a function of z_{850} magnitude between the 4 classifiers. The dashed lines represent the average RMS scatter.

As we wish to measure the MDR and MRR in forms that can be compared to previous work, we attempt to provide a standard Hubble type classification (E, S0, or Sp+Ir) for all galaxies above our flux limits. We do make a separate note on whether the object appears to be undergoing a merger or tidal disruption and the analyses of the distribution and frequency of such systems will be presented in a separate paper (Bartko et al. 2005). However, for the present work, we do not classify galaxies as merger/peculiar systems (as done by van Dokkum et al. 2000; hereafter referred to as vD2000) if one of the above standard morphological categories can indeed be applied to the individual objects involved in the merger. Nonetheless, the WFPC2 study of MS1054-0321 by vD2000 provides an additional check on the ro-

bustness of our morphological classifications. There are a total of 79 galaxies in common that have morphological classifications by us and by vD2000. Of these, 16 are classified as *M/P* (merger/peculiar) by vD2000. We classify 13 of them as bulge-dominated systems (E, S0, or S0/Sa) and 3 as later-type spiral galaxies. The ACS cutouts of these 16 objects are displayed in Figure 8. As can be seen from this figure, the morphology of most of the systems classified as mergers/peculiar by vD2000 can also reasonably be placed into one of the E/S0/Sp+Irr bins. While this confirms the vD2000 conclusion that MS1054-0321 hosts a significant fraction of early-type mergers, it does yield one difference (albeit perhaps a semantic one) in the conclusions reached regarding the overall early-type populations in MS1054-0321. By counting merg-

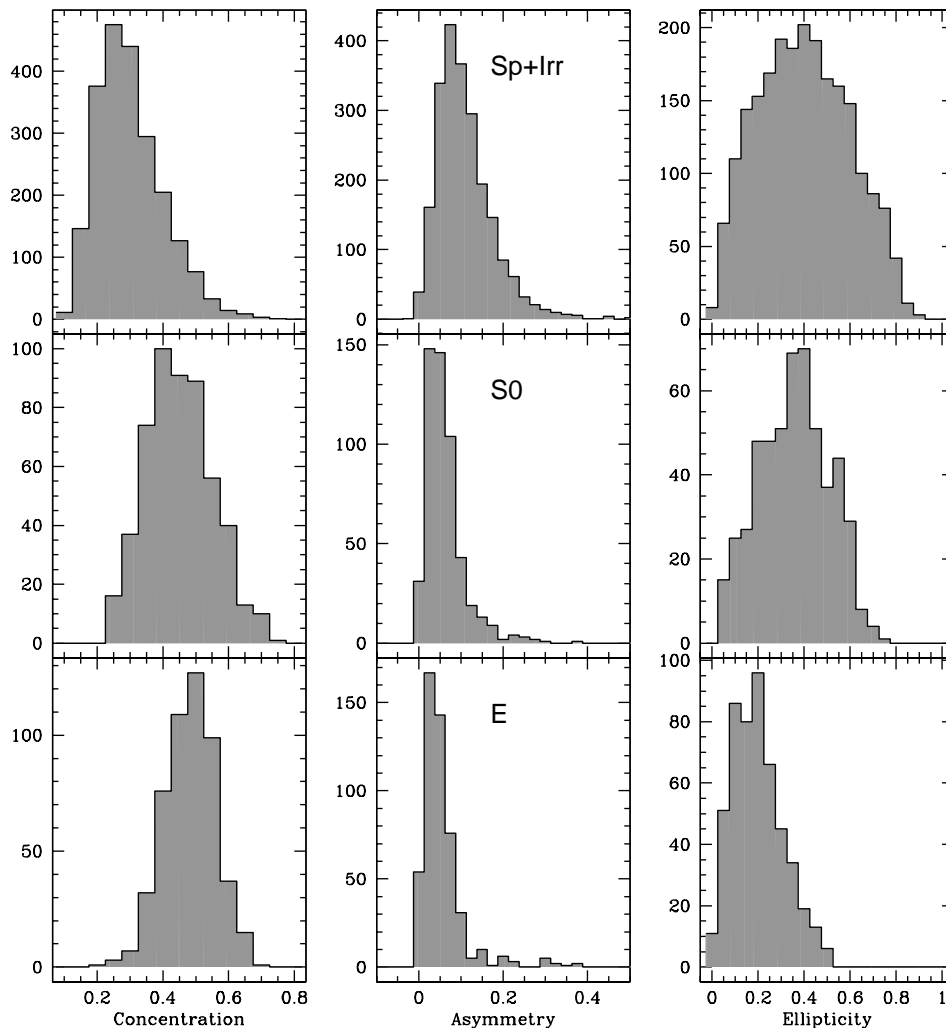


FIG. 5.— The image concentration, rotational asymmetry, and ellipticity distributions for galaxies visually classified as elliptical, S0, and Sp+Irr. The top row shows the distributions for Sp+Irr. The central row shows the S0 distributions. The bottom row shows the distributions for ellipticals.

ers/peculiar systems as a separate category, vD2000 concluded that early-type systems comprise a lower population fraction (44%) than in comparably rich clusters at lower redshift. We conclude that the early-type fraction, f_{E+S0} , in MS1054-0321 is higher – about 73%, when one attempts to classify cluster members (including merger components) as E, S0, or Sp+Irr. Of course, the factor is a function of local density and the above value is averaged over densities in the range $15 < \Sigma \leq 1000$ galaxies Mpc^{-2} . Given that the merger/peculiar category has not routinely been used in the classification of low- z clusters, we feel it is an important exercise to provide a set of morphological classifications that are as similar as possible to the low- z studies. We also agree, however, that quantifying the frequency of mergers at higher redshift reveals fundamental information about the evolution of cluster galaxies. The assessment of the early-type population component of MS1054-0321 by us and vD2000 are ulti-

mately consistent, however, if one accounts for the observation that the majority of the close pairs in MS1054-0321 include at least one bulge-dominated member.

We compare our Hubble classifications with those galaxies that vD2000 did classify as E, S0, or Spiral/Irr (i.e., excluding the M/P objects). We find exact agreement with their Hubble classification (when binned into these 3 categories) 71% of the time. We swapped E or S0 classifications 11% of the time (i.e., they called it E and we called it S0 or vice versa) and we swapped S0 and Spiral classifications 10% of the time. The remaining 8% were cases where either we or they could not make a definitive classification. This translates to a ± 0.1 scatter between our respective f_E or f_{S0} values, which is consistent with the scatter estimated from our comparisons between our ACS team classifiers.

As a further external validation of our morphological classifications, MP classified all galaxies from our

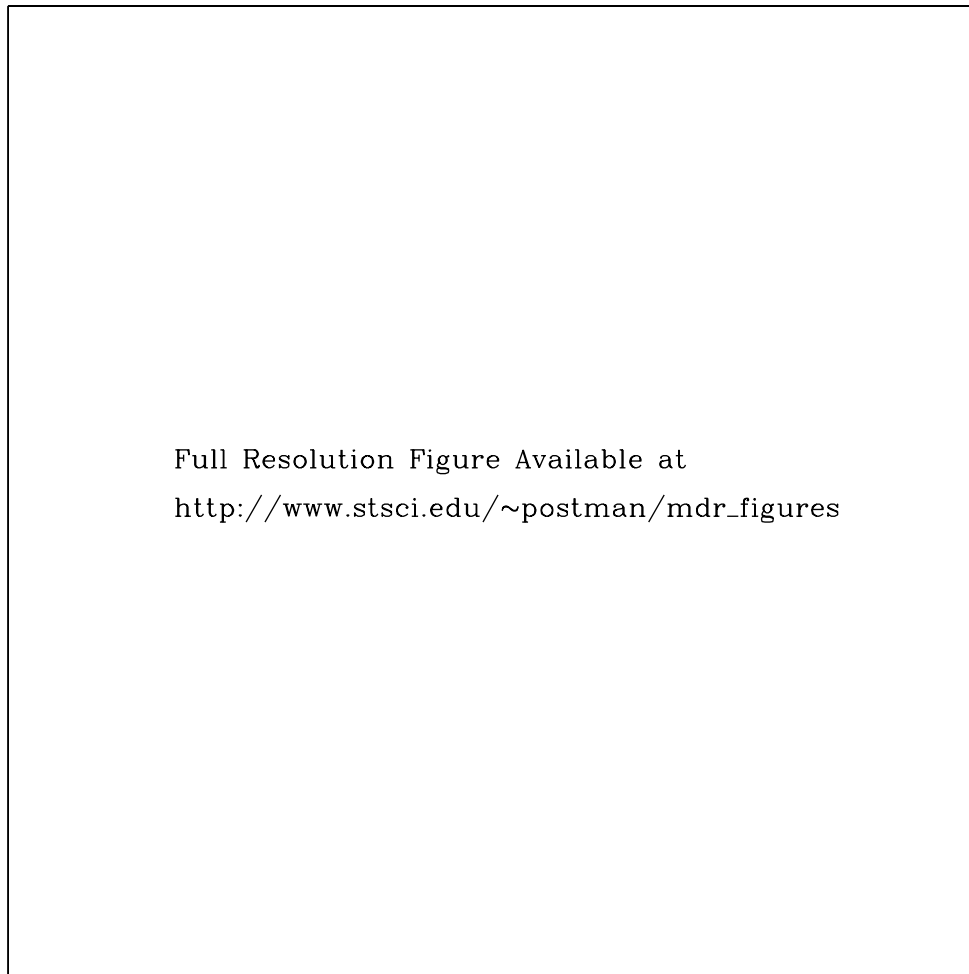


FIG. 6.— Image cutouts of 21 original ($z = 0.83$) and redshifted ($z = 1.24$) MS1054-0321 galaxies and their corresponding morphological classifications. The original image is on the left. The galaxies shown here are spectroscopically confirmed cluster members. The redshifted images are constructed to match the exposure level used for our z_{850} mosaic of RDCS1252-2927 (see Table 1).

ACS exposure of MS1358+6245 ($z = 0.33$) that were in common with the extensive study of this system performed by Fabricant et al. (2000). Agreement between the MP classifications and those from Fabricant et al. was achieved $\sim 80\%$ of the time with no systematic bias seen in the discrepant classifications (see Figure 7). We thus conclude that our E, S0, and Sp+Irr classification scheme is robust and produces Hubble types that are comparable in accuracy to visual morphological data used in other studies.

3.2. Field Morphological Population Fractions

Figure 9 shows the E, S0, and Sp+Irr fractions as a function of z_{850} for galaxies either in the field. The data points are the fractions derived from our ACS data and our visual classifications. The results in this figure are based exclusively on galaxies with spectroscopic or photometric redshifts that are incompatible with their be-

ing cluster members. The grey bands show the typical range in low-density population fractions derived from local galaxy redshift surveys (*e.g.*, PG84, D97, Goto et al. 2003a). The local ($z < 0.1$) and distant ($0.5 \lesssim z \lesssim 1$) field (*i.e.*, low-density) galaxy populations appear to have similar fractions of E, S0, and Sp+Irr systems.

4. LOCAL PROJECTED GALAXY DENSITY ESTIMATION

We compute the local projected galaxy density in two different ways to ensure robustness - the nearest N neighbors approach used by D80 and D97 and a friends-of-friends algorithm. Both methods yield consistent results and we therefore present our results in terms of the nearest N neighbors based density unless otherwise specified. Appendix A provides a demonstration of the consistency of these two density estimation techniques. In the nearest neighbor method, one computes the area of the region containing the N nearest neighbors and then derives the

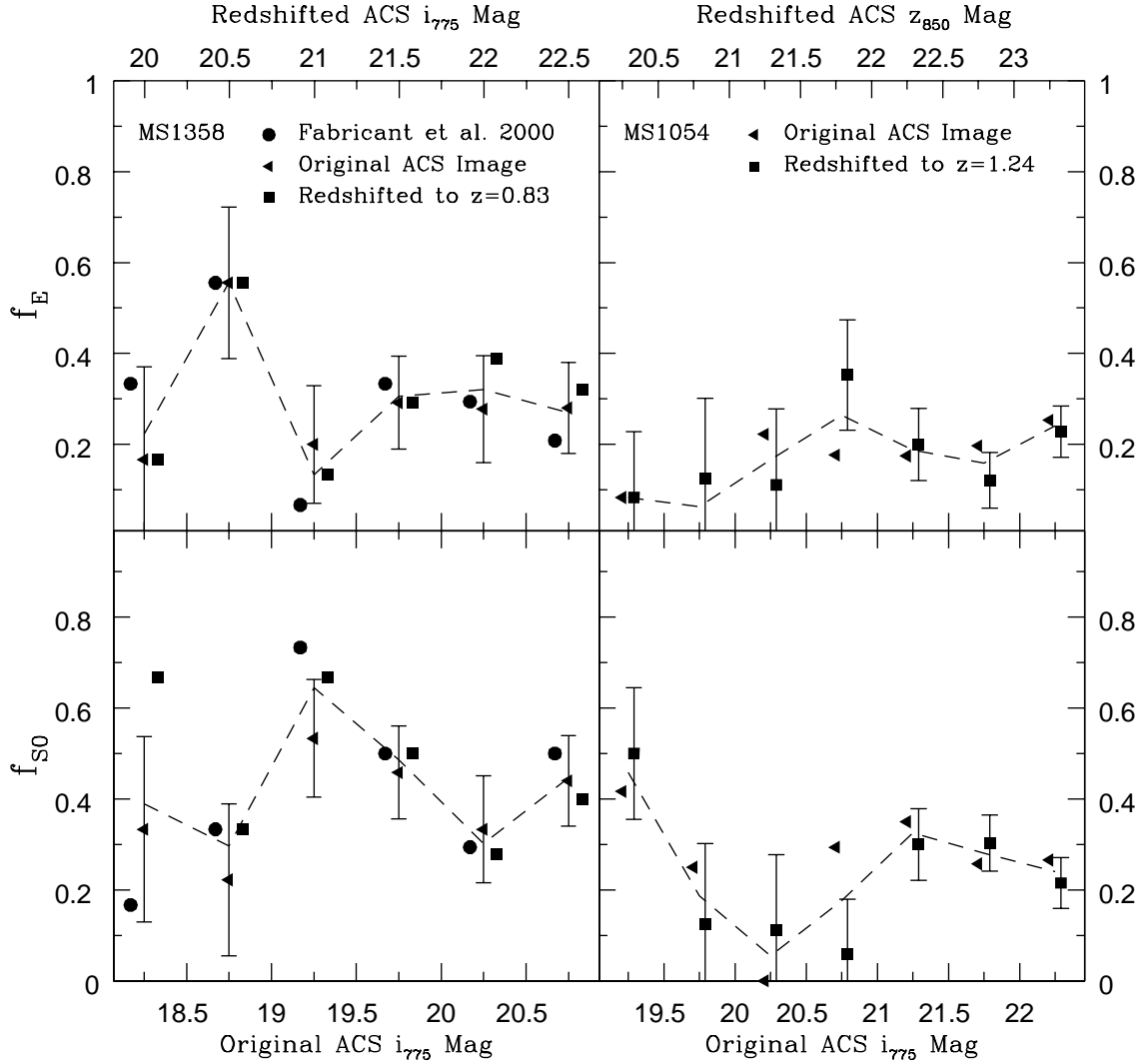


FIG. 7.— **Left Panels:** The population fractions of E and S0 galaxies as a function of i_{775} magnitude for the cluster MS1358+6245 at $z = 0.33$. The population fractions shown are from Fabricant et al. (2003) (based on their WFPC2 mosaic), and from this paper (based on the i_{775} ACS WFC image and a redshifted version of this image out to $z = 0.83$). There are no obvious systematic offsets between our fractions and those in Fabricant et al. nor any systematic changes as we redshift the data out to $z = 0.83$. The dashed lines show the population fractions obtained by averaging the results of all classifiers. **Right Panels:** The population fractions in the original MS1054-0321 ACS image and in a version redshifted to $z = 1.24$. The population fractions at each magnitude are offset from one another by a small amount for clarity.

corresponding projected density at each galaxy location from the expression:

$$\Sigma_i = \frac{f_{corr}(M_{CL}, M_{Ref})}{(\Omega_N D_A^2)} \left(\sum_{k=1}^{N+1} (w(m_k, c_k)^{-1}) - N_{bgd} \right) \quad (1)$$

where Σ_i is the projected galaxy density about a given galaxy, $f_{corr}(M_{CL}, M_{Ref})$ is a correction factor that ensures the density is always measured with respect to a common fiducial luminosity that corresponds to that used in low-redshift studies of the MDR, N is the number of nearest neighbors, $w(m_k, c_k)$ is the selection function (that can depend on magnitude and color – see Appendix B for details), N_{bgd} is a background contamination correction (if needed), Ω_N is the solid angle of the

region containing the N nearest neighbors (a rectangular region in our implementation), and D_A is proportional to the angular diameter distance to the cluster (essentially the conversion between arcsec and projected Mpc). The correction factor is

$$f_{corr}(M_{CL}, M_{Ref}) = \frac{\int_{-\infty}^{M_{Ref}} \Phi(M) dM}{\int_{-\infty}^{M_{CL}} \Phi(M) dM} \quad (2)$$

where M_{Ref} is the absolute magnitude limit to which we measure all densities, M_{CL} is the available limit for the cluster being analyzed, and $\Phi(M)$ is the galaxy luminosity function (with $M_V^*(z=0) = -21.28$ and $\alpha = -1.22$). We choose M_{Ref} to match that of the original D80 study at $z = 0$ ($M_V = -19.27$ for our

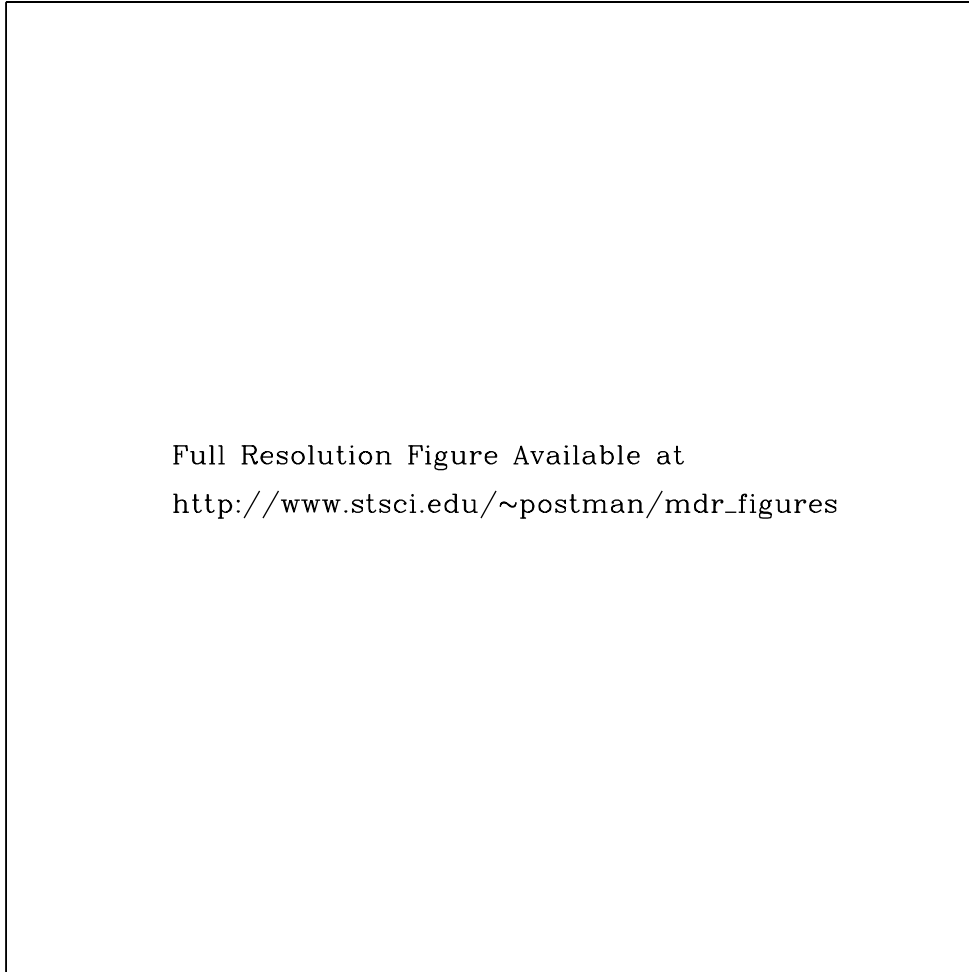


FIG. 8.— Color composite images of the 16 galaxies in common between our morphological sample for MS1054-0321 and those classified as Merger/Peculiar by van Dokkum et al. (2000). Our morphological classification of the object centered in each cutout is indicated in the lower left corner. The pictures here are made from the V_{606} , i_{775} , and z_{850} ACS/WFC images.

adopted cosmological parameters) but as we are sampling lookback times over which significant evolution in the characteristic magnitude of a Schechter luminosity function is detected, we allow M_{Ref} to vary with redshift as $M_{Ref}(z) = M_{Ref}(z = 0) - 0.8z$. For our data, f_{corr} lies in the range [1.2,3.0]. We use the density derived from the $N = 7$ nearest neighbors but the results are not sensitive to this choice in the range $5 \leq N \leq 10$.

The background correction is applied only when we are using samples requiring a statistical background subtraction. For samples based on spectroscopic or photometric redshifts, the background subtraction (if needed at all) is computed using the prescriptions described in Appendix B. Our statistical background correction, N_{bgd} , is derived from a combination of ACS and ground-based data. We use ACS observations of the HDF and Tadpole Galaxy (Benítez et al. 2004) to generate the surface density of field galaxies when $i_{775} > 23.0$. For $i_{775} \leq 23.0$,

we transform the number counts from the large I -band survey of Postman et al. (1998b) to the required ACS bandpasses.

Density estimation is most accurate when using galaxy samples that are based on spectroscopic or photometric redshift information as fore/background objects are effectively excluded from the analyses. In cases where sufficient redshift information is not available, one can use statistically-subtracted background corrected density estimates. Such estimates are only reliable in dense regions (> 80 galaxies Mpc^{-2}) where the cluster population dominates the counts. For reference, the 1σ error in the field galaxy surface density at $z_{850}=24$ is 5.4 galaxies arcmin^{-2} , which corresponds to a projected density of 26 and 22 galaxies Mpc^{-2} at $z = 0.83$ and $z = 1.27$, respectively. The statistically-subtracted background corrected population fractions and densities can be biased if there happens to be a significant overdensity in the line of

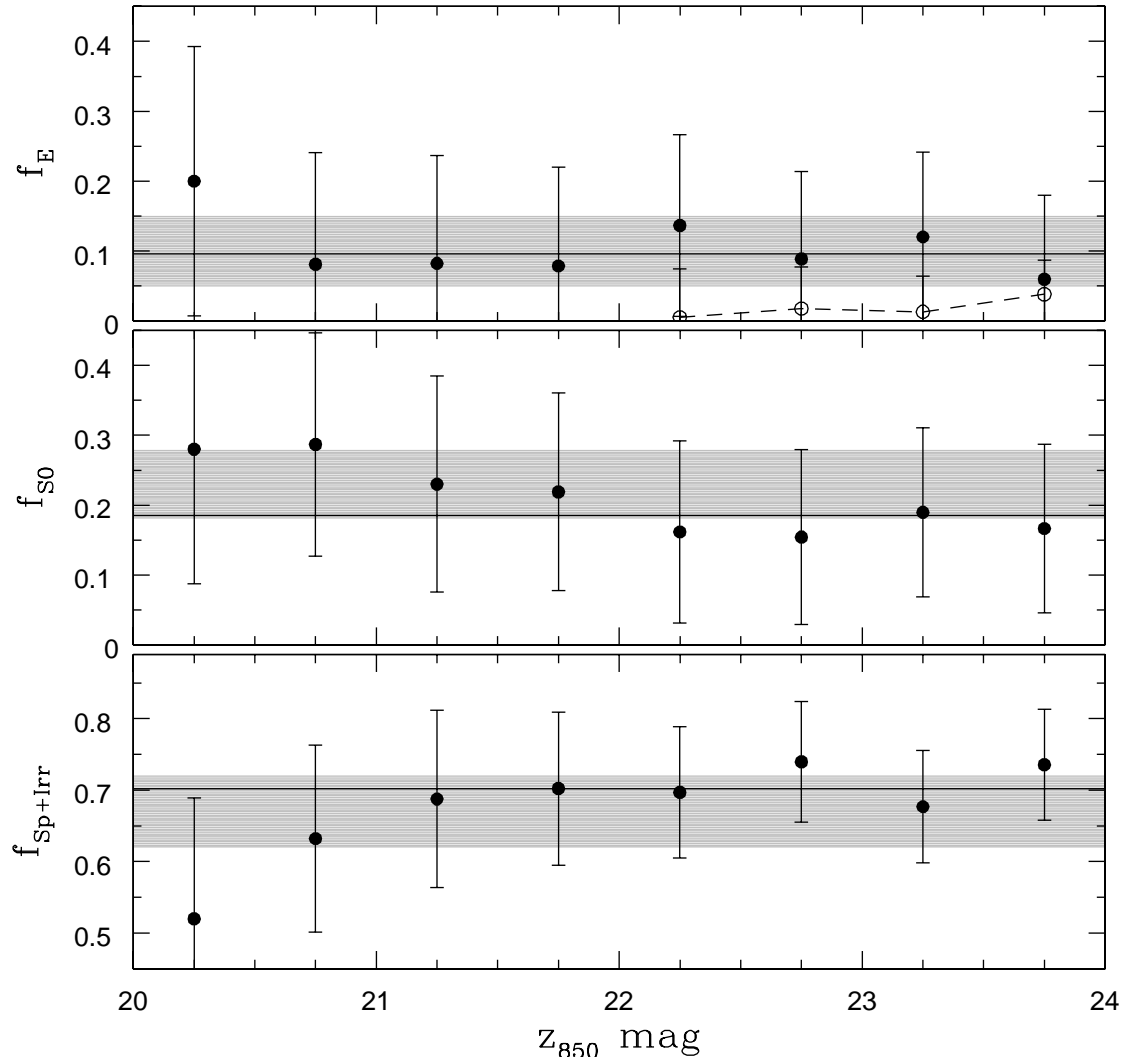


FIG. 9.— The population fractions of E, S0, and Sp+Irr of field galaxies (in our survey) as a function of z_{850} magnitude. The horizontal lines show the mean values over the range $20 \leq z_{850} \leq 24$. The grey shaded regions denote the local ($z \lesssim 0.15$) population fractions at low density ($\Sigma \lesssim 0.1$ galaxies Mpc^{-2}). The open circles in the upper plot show the fraction of galaxies for which classifications could not be readily made.

sight to the cluster. Thus, the most reliable results are those based on samples with complete or nearly complete spectroscopic or photometric redshift information. In Appendix A we demonstrate that a reliable composite MDR or MRR can be derived from a combination of spectroscopic samples, photo-z samples, and samples with statistically subtracted background corrections providing each such sample is limited to its optimal density regime.

5. THE MORPHOLOGY – DENSITY AND MORPHOLOGY – RADIUS RELATIONS AT $Z \sim 1$

We present our MDR and MRR results in Figures 10 through 15. Figure 10 shows the composite MDR derived from all clusters in the sample using the best available data. The composite MDR is derived from the spectroscopic samples for MS1054-0321 and RXJ0152-1357 for

densities below 1000 galaxies Mpc^{-2} and their photo-z selected samples for densities above 1000 galaxies Mpc^{-2} , the photo-z sample for RDCS1252-2927 (for all densities), and the statistically subtracted background results for CL1604+4304, CL1604+4321, RDCS0910+5422, and RXJ0849+4452. The statistically subtracted background results are used only when $\Sigma \geq 80$ galaxies Mpc^{-2} (roughly 3 times the amplitude of the typical fluctuations in the surface density of fore/background galaxies; see section 4). As in Sm04, we find that the MDR exists at $z \sim 1$. The $z \sim 1$ MDR results from Sm04 are shown for comparison. Our f_{E+S0} vs. local density results are consistent with those of Sm04 to within the 1σ uncertainties: we also find a less rapid increase in f_{E+S0} with increasing density than is seen at low redshift. However, the elliptical fraction, f_E , shows no significant departures from the low redshift f_E -density relation –

although, as demonstrated in Figure 4, the classification uncertainties in our f_E and f_{S0} values are about twice as high as the uncertainties in our f_{E+S0} and f_{Sp+Irr} values. The most notable difference between our current results and those at $z \lesssim 0.2$ (*e.g.*, see Figure 9 in Fasano et al. 2000) is the significantly lower fraction of S0 galaxies: averaged over all densities with $\Sigma \geq 30$ galaxies Mpc^{-2} , our mean $f_{S0} = 0.20 \pm 0.12$ where the error includes both the uncertainties from counting statistics (± 0.035) and classification errors (± 0.11). The typical low- z f_{S0} value, when averaged over the same density range, is 0.46 ± 0.06 (D80, D97, PG84) – a factor of ~ 2 higher than what is found at $z \sim 1$. A significant decline in the S0 population, relative to that seen in the current epoch, has previously been reported at redshifts as low as $z \sim 0.4$ (D97, Fasano et al. 2000). Furthermore, over the range of densities being probed in this study, f_{S0} exhibits only a weak dependence on the projected density, analogous to what is seen at similar projected densities at lower redshifts (*e.g.*, D97). The shallower growth of f_{E+S0} with increasing density seen at $z \sim 1$ by Sm04 and by us thus appears to be due to a significant deficit of S0 galaxies and an excess of spiral galaxies relative to similar environments in the current epoch. This provides further support for observations suggesting that it is the S0 and spiral population fractions that are experiencing the most significant changes with time over the past 8 Gyr (*e.g.*, Moss & Whittle 2000; Fasano et al. 2000; Kodama & Smail 2001; Treu et al. 2003; Sm04).

Figure 11 shows the morphology – radius relation (MRR) for the same composite cluster sample used in deriving the MDR in Figure 10. For each cluster we have computed an estimate of r_{200} , the radius containing a mean overdensity of 200 relative to a critical universe, based on equation 8 in Carlberg, Yee, & Ellingson (1997). The derived r_{200} values are listed in Table 2. For RDCS0910+5422 and RXJ0848+4452, we assume $\sigma = 750 \text{ km s}^{-1}$. We still need to define a cluster center for each system and for that we use the centroid of the X-ray surface brightness distribution. X-ray imaging in which the hot ICM is detected with adequate S/N levels is available for all clusters except CL1604+4321. For CL1604+4321, we use the centroid of the distribution of spectroscopically confirmed members. In the case of RXJ0152-1357, the X-ray distribution shows two well separated peaks (Della Ceca et al. 2000) and we thus subdivide the data for this cluster into two separate samples – a NE and SW component – and measure the radial distance of cluster galaxies in each subsample relative to the nearest X-ray peak. The low- z reference for the MRR is taken from Whitmore & Gilmore (1991), with their radii converted to r_{200} units using our cosmology and assuming a mean cluster redshift of $z = 0.04$ and a mean cluster velocity dispersion of 750 km s^{-1} . To aid in the comparison between the MDR and the MRR, we provide the approximate projected density – radius relationship $\log_{10}(\Sigma/635) \approx -1.63(r/r_{200})$, which is derived from our data. This approximate relation is not particularly accurate for radii less than $0.2r_{200}$ and the cluster-to-cluster variation about this relation is substantial (factors of 2–4 variation in the projected density at a given r_{200} -scaled radius), which is not surprising given the asymmetric galaxy distributions in many of our $z > 0.8$ clusters (*e.g.*, Figure 1). The key features of the MRR at $z \sim 1$ are that

(1) the bulk of the transition from a f_{Sp+Irr} consistent with that in the field environment to its minimum value occurs within $0.6 r_{200}$ ($0.6 \times r_{200}$ corresponds to physical radii of 550 kpc – 1.1 Mpc for these clusters), (2) the $z \sim 1$ f_{E+S0} value, at a given radius, is systematically less than the low- z f_{E+S0} for $(r/r_{200}) \lesssim 1.0$, and (3) the f_{S0} – radius relation shows the most significant difference from the current epoch relationship. All of these characteristics are consistent with those inferred from the $z \sim 1$ MDR. Given the significant asymmetry of the galaxy distributions in some of these clusters, however, it is likely that the MRR is being diluted and is, thus, not as clean an indicator of morphological population gradients as the MDR for this particular cluster sample.

5.1. Evolution of the Morphology–Density Relation

An additional way to assess the presence of S0 galaxies in clusters is to characterize the E+S0 ellipticity distribution, as was done by D97. As shown earlier in Figure 5, the ellipticity distributions of lenticular and elliptical galaxies differ substantially. For the full ACS galaxy sample shown in Figure 5, the hypothesis that the E and S0 ellipticity distributions are drawn from the same parent population is rejected at greater than the 99.999% confidence level. Thus, if the $z \sim 1$ bulge-dominated cluster galaxy population were truly devoid of a significant population of S0 galaxies, the ellipticity distribution of the E+S0 galaxies would more closely resemble that of pure ellipticals and would not include a significant component of objects with ellipticities beyond 0.5. Figure 12 shows the ellipticity distributions of the E+S0 cluster galaxy populations for three of our $z > 0.8$ cluster galaxies along with galaxies from five clusters with redshifts in the range $0.25 \leq z \leq 0.55$. To make a fair comparison of these two cluster samples, we must select objects that lie in similarly dense environments. Therefore, the galaxies used in this comparison are all selected from environments where the local projected density is ≥ 100 galaxies Mpc^{-2} . The $z > 0.8$ sample used here consists of the photo- z selected cluster members in RXJ0152-1357, MS1054-0321, and RDCS1252-2927. We limit the $z > 0.8$ cluster sample to the three clusters with good photo- z data to ensure we are selecting probable cluster members. The $z < 0.6$ cluster data are from GTO ACS observations of 5 strongly lensing clusters in the range $0.25 \leq z \leq 0.55$ (HST PID #9292). The 5 clusters are Zw1455+2232 ($z = 0.258$), MS1008–1224 ($z = 0.301$), MS1358+6245 ($z = 0.328$), CL0016+1654 ($z = 0.54$), and MS J0454-0300 ($z = 0.55$). Visual classification of all galaxies with $i_{775} \leq 22.5$ in each $z < 0.6$ cluster ACS image was performed by MP. The rest-frame wavelengths sampled by the i_{775} filter for $0.25 \leq z \leq 0.55$ typically lie in the V -band, thus any “morphological” k -corrections between this sample and the $z > 0.8$ sample should be small. A total of 798 galaxies were classified in the five $z < 0.6$ clusters. As the low- z ACS images were all single pointings centered on the cluster core, the vast majority of the E and S0 galaxies identified are likely to be cluster members. For reference, the ACS/WFC subtends 800 kpc at $z = 0.26$ and 1.3 Mpc at $z = 0.55$. A Kolmogorov-Smirnov test finds that the distribution of ellipticities of E+S0 galaxies in the $z > 0.8$ clusters is inconsistent with being drawn from a pure elliptical ellipticity distribution at the 97.0% confidence level. A

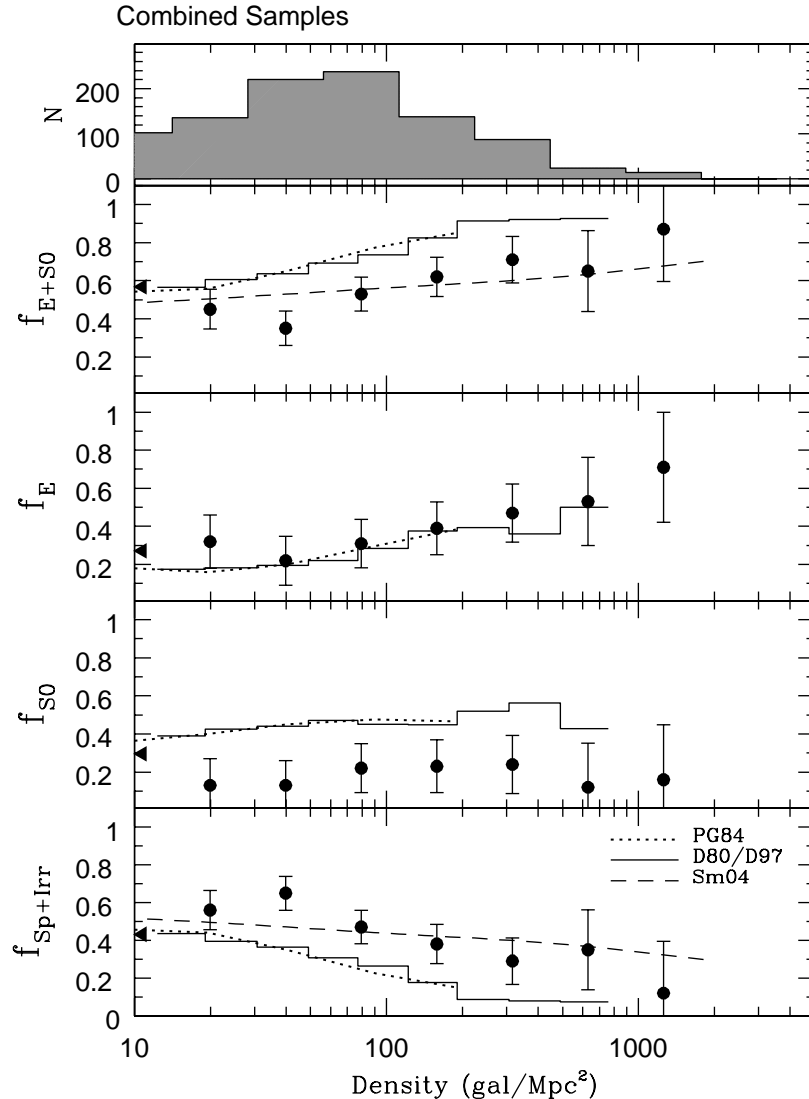


FIG. 10.— The MDR for all clusters based on the best available data. See text for details. Errorbars include the uncertainties in counting statistics and morphological classification. The previous results from low- z surveys (D80, D97, PG84, SDSS) and from $z \sim 1$ (Sm04) are shown for reference. The triangular markers along the y-axis show the low-density population fractions from the SDSS (Goto et al. 2003a).

Wilcoxon rank-sum test, which is better suited to measuring differences in the mean values of two distributions than a KS test, finds the E+S0 and E galaxy distributions for the $z > 0.8$ clusters differ at the 3.1σ level. We thus reject the hypothesis that there are no S0 galaxies in dense environments at $z \sim 1$. The E+S0 and E galaxy ellipticity distributions for the $0.25 \leq z \leq 0.55$ cluster sample are inconsistent with each other at the 99.998% confidence level.

We can also apply a robust test (*i.e.*, one that primarily relies on our ability to distinguish only between E+S0 and Sp+Irr) in an attempt to constrain the evolution of the S0 population by comparing the $z > 0.8$ E+S0 ellipticity distribution with that for the $0.25 \leq z \leq 0.55$ cluster galaxy sample. The cumulative distribution functions for the E+S0 ellipticities in the two different cluster samples are shown in the top panel in Figure 12. The ellipticity distributions for the $0.25 \leq z \leq 0.55$ and the

$z > 0.8$ cluster samples are, however, completely consistent with one another (KS test rejects inconsistency only at the $\sim 10\%$ confidence level), suggesting that, at least in these particular samples, any evolution in the relative E and S0 population fractions does not manifest itself as a significant difference in the E+S0 ellipticity distribution. It is possible that with larger and more homogeneously selected cluster samples over a range of redshifts this test would provide a quite objective way to measure the evolution of the morphological population fraction in dense environments.

The f_{E+S0} as a function of lookback time and local density is shown in Figure 13. This figure is modeled after Figure 3 in Sm04. The Sm04 results are reproduced for reference in the lower panel of Figure 13. The upper panel of Figure 13 shows the analogous results for our ACS $z > 0.8$ and $0.25 \leq z \leq 0.55$ cluster samples. The results in the upper panel are based on the mean popu-

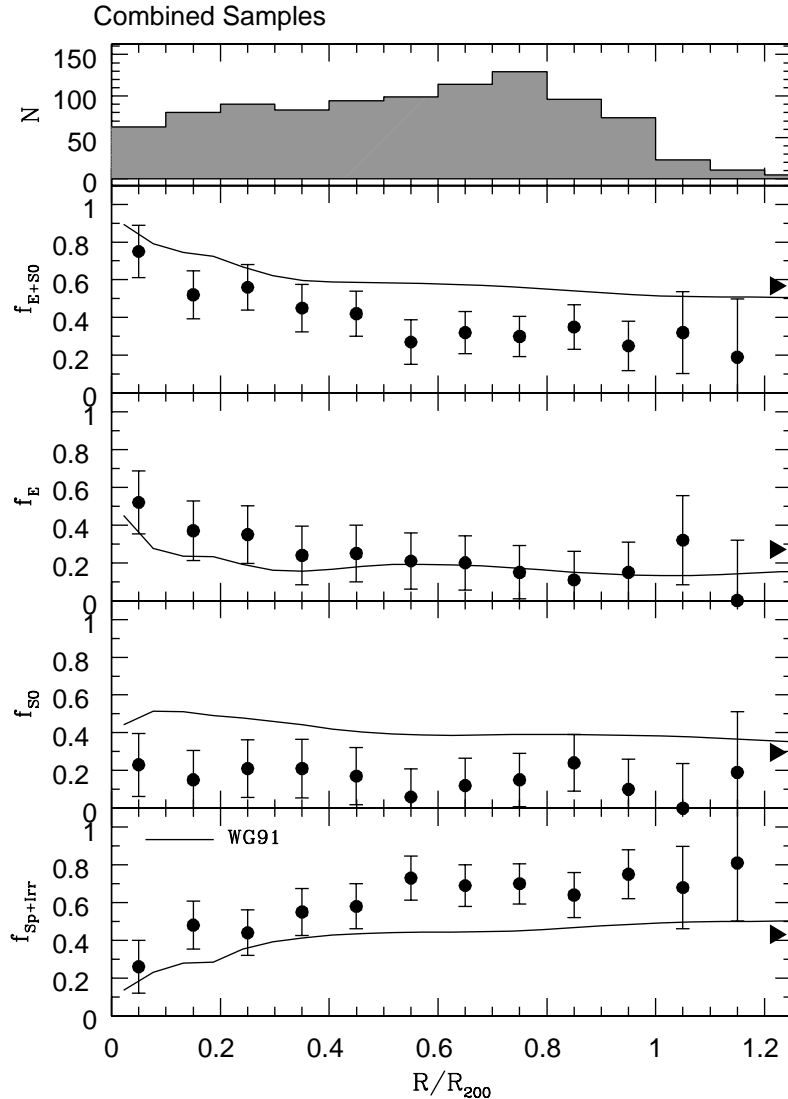


FIG. 11.— The Morphology – Radius relation for all clusters based on the best available data. See text for details. Errorbars include the uncertainties in counting statistics and morphological classification. Cluster centers are determined from the centroid of the X-ray surface brightness distribution except for CL1604+4321, where the centroid of the distribution of confirmed spectroscopic members is used instead. The solid line is the low- z morphology – radius relation from Whitmore & Gilmore (1991), converted to r_{200} units assuming a mean cluster redshift of $z = 0.04$ and a mean cluster velocity dispersion of 750 km s^{-1} . The triangular markers along the y-axis show the low-density population fractions from the SDSS (Goto et al. 2003a).

lation fractions within logarithmic density bins 0.4 units wide centered at 10, 100, and $1000 h_{65}^2 \text{ galaxies Mpc}^{-2}$. Our f_{E+S0} values are in good agreement with the Sm04 values - any differences are comparable with the uncertainties. We corroborate the key observational result of the Sm04 study that the most significant differences between the MDR at low redshift and high redshift are confined to regions where the projected galaxy density is larger than $\sim 40 \text{ galaxies Mpc}^{-2}$. While the agreement is re-assuring given the significant overlap of the clusters used in the two programs, and bolsters the concept of using visual morphological classification in comparative studies at high- z , there is also significant room for reducing the existing uncertainties that will be achieved only when a much ($\sim 10\times$) larger sample of $z \sim 1$ cluster

galaxy morphologies is available. Our derived population fractions as a functions of projected density and radius are also provided in Tables 3 and 4 for easy reference. As noted above, our results suggest that the observed MDR evolution is primarily driven by evolution in the fractions of S0 and Sp+Irr galaxies.

5.2. A Correlation between f_{E+S0} and L_x ?

Our sample exhibits a potentially interesting trend between the early type population fraction and the cluster bolometric X-ray luminosity. The bulge-dominated galaxy population fraction in clusters with high X-ray luminosity ($L_{x,\text{Bol}} \geq 1.5 \times 10^{45} h_{70}^{-2} \text{ erg s}^{-1}$) is higher than that in low X-ray luminosity ($L_{x,\text{Bol}} \leq 3 \times 10^{44} h_{70}^{-2} \text{ erg s}^{-1}$) clusters, even at the highest projected densities.

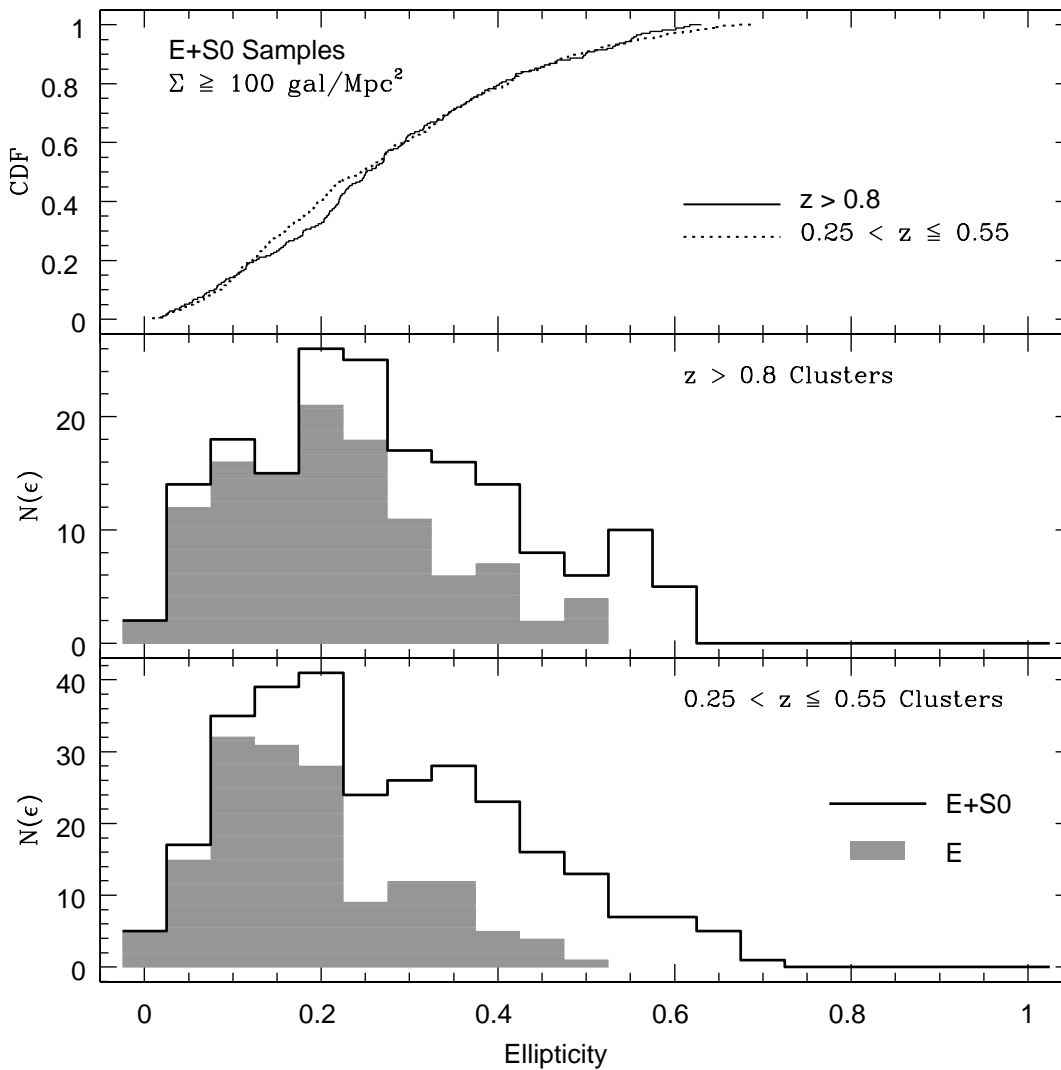


FIG. 12.— The distribution of ellipticities for the bulge-dominated galaxies that are likely cluster members in 2 different redshift ranges. The lower redshift cluster data are also based on ACS imaging and come from observations of 5 strongly lensing clusters in the range $0.25 \leq z \leq 0.55$. See section 6 for details. The $z > 0.8$ galaxies are from our photometric redshift sample for the clusters RXJ0152-1357, MS1054-0321, and RDCS1252-2927. The E+S0 ellipticity histograms are drawn with thick lines. The elliptical galaxy ellipticity distributions are represented by the light grey shaded histograms. The uppermost panel shows the cumulative distribution functions for the ellipticities of the E+S0 galaxies in each cluster sample.

This is demonstrated in Figure 14. Here we show f_{E+S0} , f_E , and f_{S0} as a function of the bolometric X-ray luminosity for the galaxies within r_{200} for each cluster. D80 found a modest increase in f_{S0} , a corresponding decrease in f_{Sp+Irr} , and no change in f_E in his sub-sample of 8 high X-ray emitting clusters relative to the full sample of 55 clusters. Least square, error-weighted, fits to the trends in Figure 14 give

$$f_{E+S0} \propto L_{x,Bol}^{0.33 \pm 0.09}$$

$$f_E \propto L_{x,Bol}^{0.15 \pm 0.09}$$

$$f_{S0} \propto L_{x,Bol}^{0.18 \pm 0.09}$$

The linear correlation coefficients for the fits to the $\log(L_{x,Bol}) - f_{E+S0}$, $\log(L_{x,Bol}) - f_E$, and $\log(L_{x,Bol}) -$

f_{S0} data are 0.82 (97.6% CL), 0.84 (98.2% CL), and 0.75 (94.8% CL), respectively. The correlations are significant at the $2 - 3\sigma$ level.

A correlation between f_{E+S0} and L_x could, in principle, be produced either as a consequence of environmental interactions subsequent to the formation of the cluster galaxies and/or as a result of the initial conditions present at the time of their formation. In a simplified example of the former scenario, the ram-pressure, P_{ram} , acting on a galaxy moving through the intracluster medium (ICM) is proportional to ρv^2 . If the ICM is in hydrostatic equilibrium, then the bolometric X-ray luminosity, L_x , is proportional to $\rho^2 T_x^{1/2} R^3$ (e.g., Ettori et al. 2004). The total mass of the system, M_{tot} , is proportional to $T_x^{3/2}$ and is also proportional to v^2 . The same

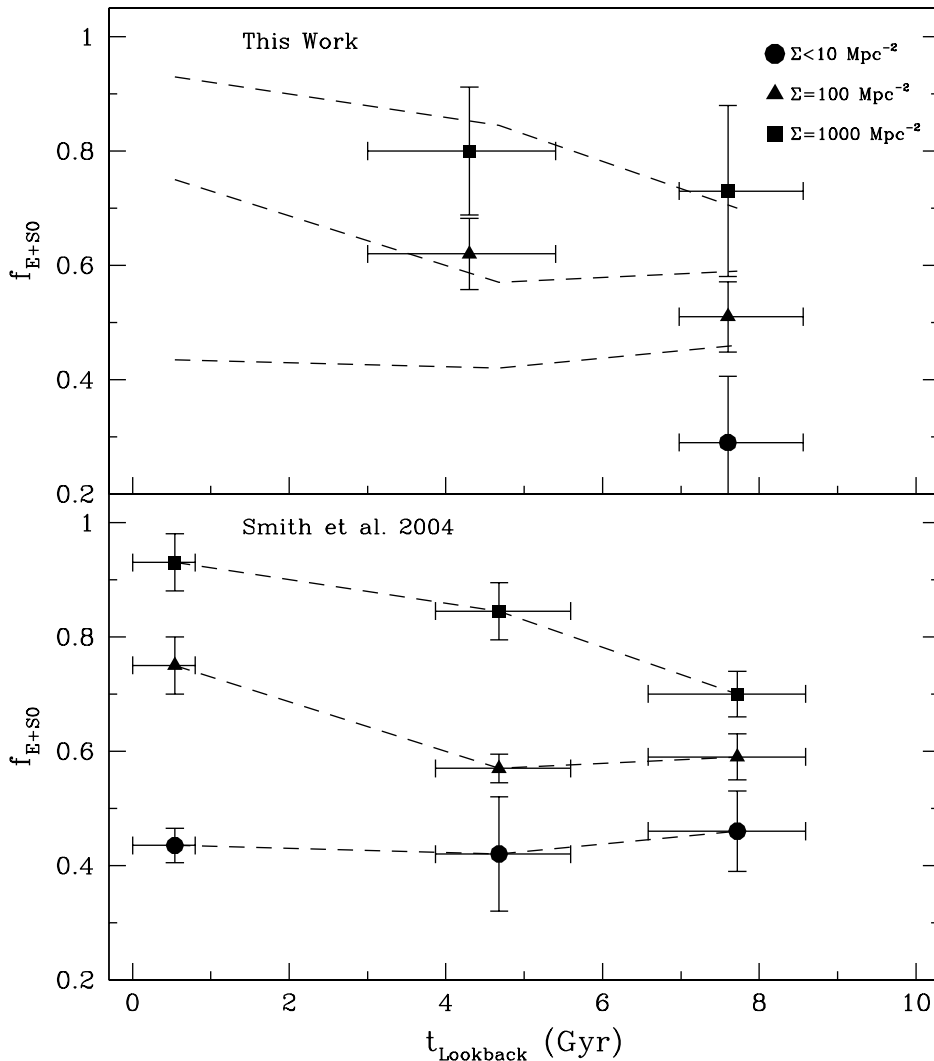


FIG. 13.— **Bottom:** The evolution of the MDR reported by Sm04. Lookback times have been transformed to compensate for the small difference between the cosmology in Sm04 and that adopted in this paper - specifically, our choice of a slightly larger Hubble constant (70 vs. 65). The dashed lines representing the change in f_{E+S0} with time at the 3 different density regimes are reproduced in all three panels for reference. **Top:** Our derived E+S0 fractions at projected densities corresponding to < 10 , 100, and $1000h_{65}^2$ galaxies Mpc^{-2} (to match Sm04) for our combined $z \sim 1$ cluster sample and our $0.25 \leq z \leq 0.55$ cluster sample. The latter sample is not suitable for measuring low-density population fractions.

family of scaling laws gives $L_x \propto T_x^2$, although observationally a steeper relation is found where $L_x \propto T_x^{2.8}$ (*e.g.*, Ponman et al. 1996; Mulchaey & Zabludoff (1998); Xue and Wu (2000)). These relations can be manipulated to yield $P_{ram} \propto L_x^{1.0 \pm 0.1}$, where the exponent value depends on the exponent in the $L_x - T_x$ relation. The ram-pressure is stronger within more luminous X-ray clusters. Therefore, if ram-pressure stripping were the dominant mechanism responsible for the origin of S0 galaxies in clusters, f_{E+S0} should exhibit a positive correlation with L_x . However, many previous observations, including the relatively weak dependence of f_{S0} on projected density, strongly suggest that ram pressure stripping alone cannot explain the morphological mix in clusters (*e.g.*, D80; D97; Kodama & Smail 2001; Okamoto & Nagashima 2003).

Alternatively, a positive correlation between f_{E+S0} and L_x could be produced as a consequence of simple dynamics - the most massive (and, hence, most X-ray luminous) clusters will collapse earlier and any environmentally-driven processes that produce bulge-dominated galaxies will therefore have been active for a longer period of time at any subsequent redshift. This simple timescale argument could result in a positive correlation between the fraction of early-type galaxies and observational proxies for cluster mass, regardless of whether or not the efficiencies of the transformation processes are correlated with the properties of the ICM. However, this would only be true if the timescales required to establish a significant population of early-type galaxies were long compared to the collapse time. If the timescale for establishing the early-type population were comparable to the

collapse time (i.e., if deeper potential wells are “born” with a higher early-type population fraction), then the $f_{E+S0} - L_x$ relation may be telling us more about cluster and galaxy formation processes than about the cluster evolution process.

As the results in Figure 14 are based on only 7 clusters and as the significance of the correlations are only significant at the $\lesssim 3\sigma$ level, we refrain from over-interpretation. Indeed, the correlations between f_{E+S0} and T_x and f_{E+S0} and cluster velocity dispersion, σ , are not significant (see Figure 15). In the literature, the mass dependence of cluster galaxy evolution has been a subject of debate. For example, Fairley et al. (2002) studied eight X-ray selected clusters and did not find any dependence of the blue galaxy fraction on L_x – a trend that might be expected if f_{E+S0} correlated with L_x . De Propris et al. (2004), using a larger sample of 60 clusters from the 2dF Galaxy Redshift Survey, finds that the blue galaxy fraction does not depend on the velocity dispersion of the cluster galaxies. However, there is tentative evidence that cluster integrated star formation rates (*e.g.*, Finn et al. 2004) correlate with T_x and L_x (Homeier et al. 2005), which is presumably a dependence on cluster mass. Furthermore, Zabludoff & Mulchaey (1998) found that groups of galaxies exhibit a strong correlation between the bulge-dominated galaxy fraction, f_{E+S0} , and the group velocity dispersion. And while the specific relation they found cannot be extended to very massive clusters (their predicted f_{E+S0} reaches a value of unity at a velocity dispersion of $\sim 700 \text{ km s}^{-1}$), it does suggest that groups of galaxies have a positive correlation between f_{E+S0} and L_x through the observational relation $L_x \propto \sigma^{4.3}$ (Mulchaey & Zabludoff 1998). Margoniner et al. (2001) and Goto et al. (2003b) find that blue fractions of cluster galaxies are lower for richer clusters, a result that is consistent with a positive $f_{E+S0} - L_x$ relationship.

The significance of the $f_{E+S0} - L_x$ relation clearly needs to be studied using a larger sample so that subdivision by mass (or a suitable observational proxy for mass) can be conducted for a far greater number of clusters. The HST/ACS snapshot program of 73 homogeneously selected X-ray clusters (ID#10152, M. Donahue, P.I.) should provide the sample needed to assess this relation in the range $0.3 < z < 0.7$. If a significant $f_{E+S0} - L_x$ relation is ultimately found, one implication is that the MDR and its evolution may be dependent on the total cluster mass. Certainly on galaxy-mass scales, there is evidence that the star formation process occurs more rapidly in systems with higher stellar mass (*e.g.*, Heavens et al. 2004). For the present sample, correlations between the fraction of early type galaxies and the X-ray properties of the clusters provide, at best, a strong inspiration to study the trends with samples explicitly geared to investigate this relationship.

6. DISCUSSION

As originally discussed by Tully and Shaya (1984), the measurement of the evolution in the MDR is a significant step in understanding the relative roles of environment and initial conditions in establishing morphological population gradients. The less rapid growth in the bulge-dominated galaxy population with increasing density (or decreasing radius) that is seen at $z \sim 1$, implies that en-

vironment must play an important role in the establishment of the current epoch MDR. Sm04 explore a range of morphological transformation scenarios based on the expression:

$$f_{S0,z=1} = f_{E+S0,z=1} - f_{E,z=0.5} \frac{N_{z=0.5}}{N_{z=1}} + \frac{\Delta N_E}{N_{z=1}} \quad (3)$$

where $f_{S0,z=1}$ is the S0 population fraction in clusters at $z = 1$, $f_{E+S0,z=1}$ is the E+S0 fraction in clusters at $z = 1$, $f_{E,z=0.5}$ is the elliptical fraction in clusters at $z = 0.5$, $N_{z=0.5}/N_{z=1}$ is the ratio of the number of galaxies in clusters at $z = 0.5$ to that at $z = 1$, and ΔN_E is the change in the number of cluster ellipticals between $z = 1$ and $z = 0.5$. By combining varying amounts of infall (including infall of early-type galaxies), mergers, and cannibalism, Sm04 find that for reasonable levels of each process the f_{S0} at $z = 1$ is typically less than 0.1. The exception is for the case where there is no infall and 10% of the spiral galaxies merge in pair-wise manner to form ellipticals. In this case, the model predicts $f_{S0} = 0.18$ at $z = 1$. The degree to which our observations conflict with the predictions for very low S0 population fractions in $z = 1$ clusters is, of course, directly tied to the uncertainty in our f_{S0} measurements. Our mean S0 population fraction is inconsistent with being zero at about the 90% confidence level, which is not strongly in conflict with the Sm04 predictions for $f_{S0,z=1}$. However, given that the ellipticity distribution of the E+S0 galaxies in the $z \sim 1$ clusters is inconsistent with being drawn from a population dominated largely by pure elliptical morphologies and given that we do get a mean f_{S0} of 0.20 ± 0.12 for $\Sigma \geq 30$ galaxies Mpc^{-2} , we investigate minor variations to the Sm04 scenario that can increase in the predicted S0 population fraction at $z \sim 1$. An obvious choice is to explore reasonable modifications of the value of $f_{E,z=0.5}$. Sm04 adopted $f_{E,z=0.5} = 0.6$. However, we find that for $\Sigma \geq 100$ galaxies Mpc^{-2} a value in the range $0.4 - 0.5$ appears to be closer to what the data suggest. Decreasing $f_{E,z=0.5}$ to 0.5 increases the range of the Sm04 predictions to $0.09 \leq f_{S0,z=1} \leq 0.28$ for the models considered. This would make their predictions and our mean f_{S0} values consistent within 1σ . However, doing so does change the conclusions of Sm04 a bit - namely that $\sim 50\%$ of the lenticulars in clusters could already be in place at $z = 1$ and that the remaining half form largely between $z \sim 0.5$ and the present epoch.

Different morphological transformation mechanisms operate in different environments and, thus, by identifying the radius or density where the morphology of cluster galaxies start to change, we can hope to identify the underlying physical mechanisms. The breaks in the MDR, first characterized by PG84 and more recently by Goto et al. (2003), suggest different processes are probably responsible for the origin of elliptical and S0 galaxies. For example, ram-pressure stripping (Gunn & Gott 1972) is only efficient within the cluster core (typically $\lesssim 250$ kpc) where the ICM density is high enough to allow the dynamic pressure to overpower the gravitational restoring force of interstellar gas in a galaxy’s disk. Figure 11 indicates that the fraction of elliptical galaxies starts to increase inwards of $0.6 r_{200}$, or in terms of local galaxy density, at around 70 galaxies Mpc^{-2} (Figure 10). This environment matches that where the population fraction of Sp+Irr galaxies starts to decline. The scale of

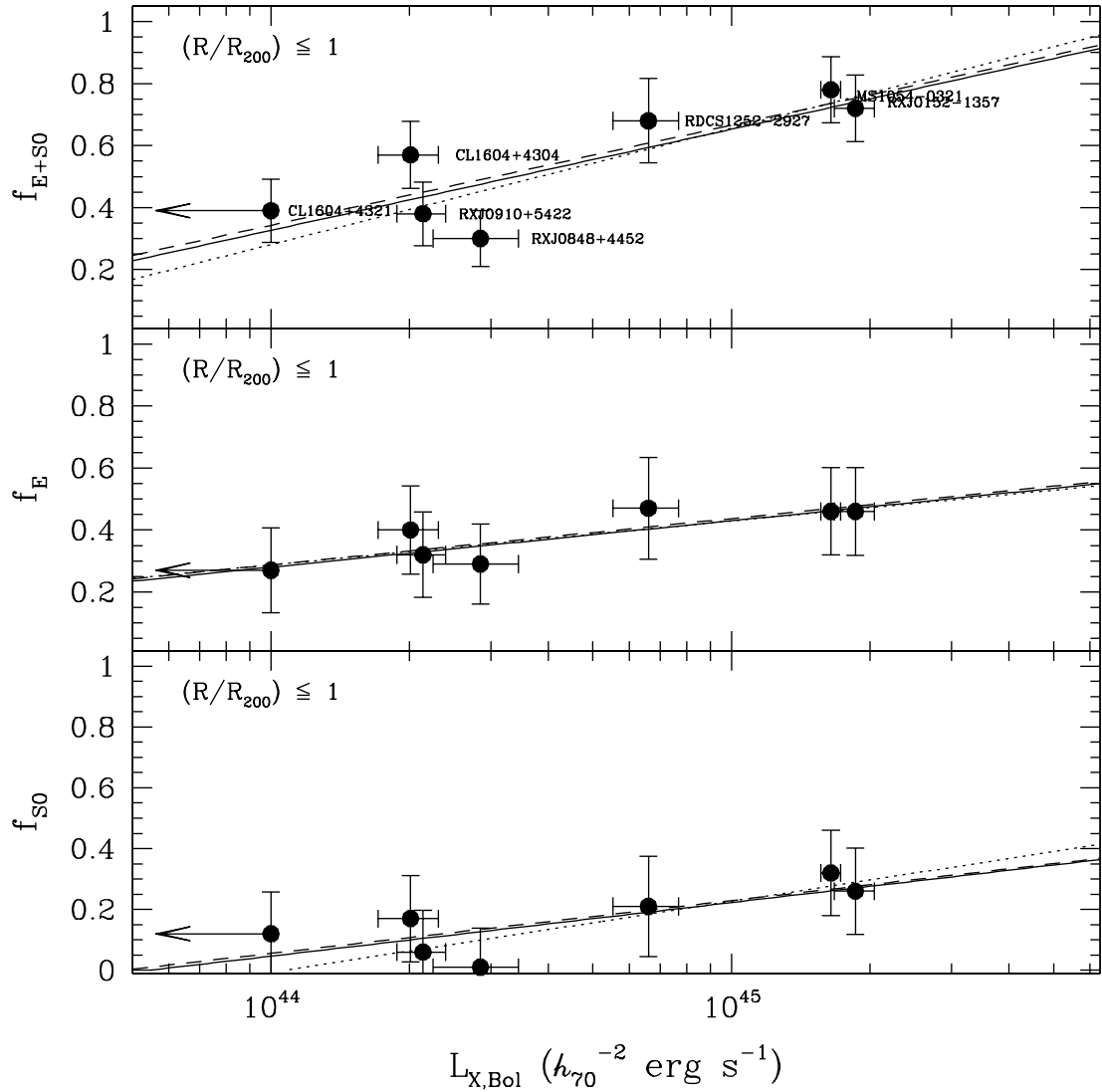


FIG. 14.— The dependence of the bulge-dominated galaxy population fractions, f_{E+S0} , f_E , and f_{S0} , on the bolometric cluster X-ray luminosity within a radius corresponding to r_{200} . Names of the individual clusters are shown in the upper panel. The solid line is the best fit relation when the data are weighted by the inverse square of their uncertainties. The dashed line is the best fit when each data point is given equal weight. The dotted line is the best error-weighted fit with CL1604+4321 excluded. The data for RXJ0152-1357 in this figure includes both the NE and SW components of the cluster. Errorbars include the uncertainties in counting statistics and morphological classification.

0.6 r_{200} for the onset of the transition between the low-density field population and that in high density regions is in agreement with previous low redshift observations (*e.g.*, Kodama et al. 2001; Treu et al. 2003; Goto et al. 2003b). At distances beyond 250 kpc or so, ram pressure becomes much less effective as a morphological transformation process and thus other environmental processes must play a significant role in the establishment of the MDR and MRR (*e.g.*, Treu et al. 2003). Galaxy-galaxy merging, for example, is most effective when relative velocity of galaxies are comparable to the rotation of galaxy itself ($\sim 200 \text{ km s}^{-1}$) and is thus likely to be most effective in regions far from the cluster core. Galaxies beyond 5 Mpc from the cluster center will, at $z \sim 1$, not yet have had sufficient time to traverse the cluster core and should, therefore, not experience tidal stripping or

tidal triggering of the star formation due to the cluster gravitational potential.

The lack of any significant redshift dependence in the f_E – density relation coupled with the significant changes with redshift seen in the f_{S0} – density relation suggest that the origin of the MDR and MRR in high density regions is most likely determined by two distinct processes: (i) formation of elliptical galaxies at the cluster core, which occurred at redshifts significantly greater than unity and (ii) the formation of S0 galaxies, which appears, for at least half of the lenticulars, to be a process that is still underway even at redshifts as low as $z \sim 0.5$. Evidence for different formation timescales for elliptical and S0 galaxies comes from other types of studies as well. For example, the analysis of the color-magnitude relation (CMR) in RDCS1252-2927 by Blakeslee et al.

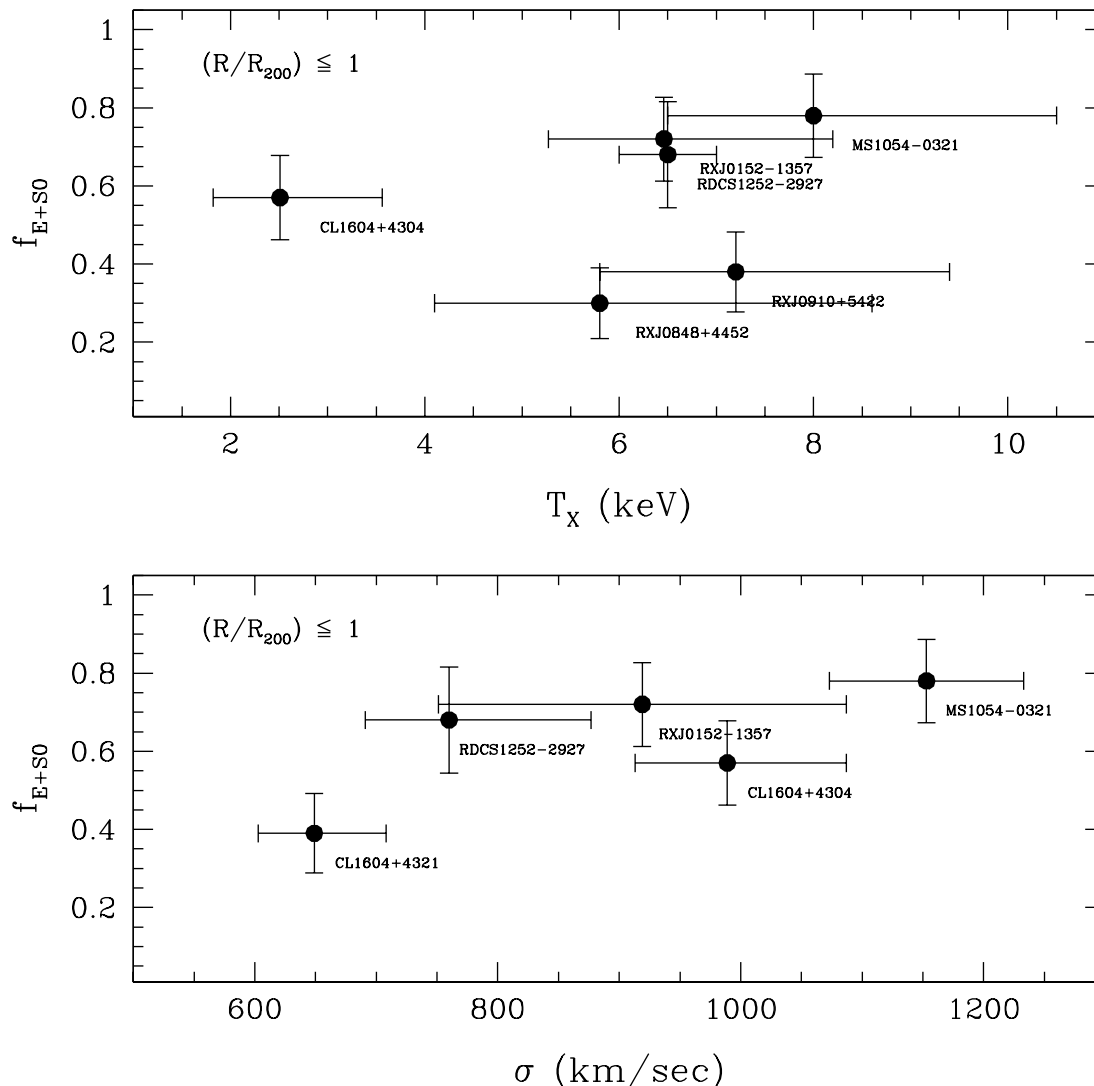


FIG. 15.— The bulge-dominated galaxy population fraction, f_{E+S0} , within a radius corresponding to r_{200} as a function of the X-ray gas temperature and cluster velocity dispersion. Names of the individual clusters are shown. Errorbars include the uncertainties in counting statistics and morphological classification.

(2003) finds that the observed scatter in the CMR for S0 galaxies in that system is consistent with relatively recent or even on-going star formation activity whereas the CMR for elliptical galaxies in this $z = 1.24$ cluster is compatible with no significant star formation activity for more than a Gyr. In addition, Poggianti et al. (1999) and Goto, Yagi, Tanaka, & Okamura (2004) derive shorter evolutionary timescales for blue to red spiral transformation than for red spiral to red elliptical transformation, consistent with the hypothesis that transformation of a galaxy's spectral energy distribution typically occurs more rapidly than morphological transformation.

A fundamental question that remains is whether or not the MDR and MRR depend on luminosity. It is well established that intrinsically luminous, red galaxies are almost always elliptical and, hence, at some level limiting the analyses of the MDR to intrinsically luminous galaxies may produce a different relationship between mor-

phology and projected density than found in a sample containing a broader range of luminosities. Tanaka et al. (2005) demonstrate that there is indeed a change in the MDR at $z < 0.07$ as a function of luminosity based on an analysis of $\sim 20,000$ SDSS galaxies. They find that galaxies fainter than $M_r^* + 1$ do appear to have a different MDR at low densities than brighter galaxies. We have divided our spectroscopic samples for MS1054-0321 and RXJ0152-1357 into four apparent magnitude ranges $i_{775} \leq 22$, $i_{775} \leq 22.5$, $i_{775} \leq 23$, and $i_{775} \leq 23.5$ corresponding to $M^* \leq M_{775}^* - 0.3$, $M^* \leq M_{775}^* + 0.2$, $M^* \leq M_{775}^* + 0.7$, and $M^* \leq M_{775}^* + 1.2$. We find no significant difference between the MDR derived for these 4 samples. If the luminosity dependence of the MDR does not exhibit strong evolution, then our current sample does not go deep enough at $z = 0.83$ to accurately measure the dependence. Our failure to detect any luminosity dependence in the MDR in our $z = 0.83$ spec-

troscopic sample is thus not inconsistent with the work done at low redshifts. Furthermore, our survey is not well suited to studying densities below 30 galaxies Mpc^{-2} , well above the density where the Tanaka et al. (2005) find the strongest luminosity-dependent effects. All we can conclude for now is that for $\Sigma > 30$ galaxies Mpc^{-2} and for $M^* \lesssim M_{775}^* + 1.2$ the $z = 0.83$ MDR is not sensitive to luminosity. The caveat to this conclusion is that our i_{775} data at $z = 0.83$ samples the rest-frame B -band. It may be that galaxies selected according to a redder rest-frame luminosity will show a different trend. The underlying goal of studying the MDR as a function of luminosity is, of course, to assess the dependence of the MDR on galaxy mass. We are assembling NIR photometry for our cluster galaxies to provide more accurate stellar mass estimates and we will explore trends between morphology, density, r_{200} , and galaxy mass in a future paper.

7. CONCLUSIONS

We have performed deep, multiband observations with the ACS/WFC of 7 clusters with $0.83 \leq z \leq 1.27$ to study the morphological composition of the galaxy population over 3 decades of local density and out to radii of up to 2 Mpc from the peak of the X-ray emission from the ICM. The key results are:

1. The high sensitivity and angular sampling of the ACS/WFC enable reliable visual distinctions to be made between the major morphological galaxy classes (E, S0, Sp+Irr) down to $\sim 0.25L/L^*$ in the range $0.8 < z < 1.3$.
2. We confirm the results of Smith et al. (2004) that a morphology – density relation exists at $z \sim 1$. We also explicitly confirm the less rapid growth in f_{E+S0} with increasing density and that the change in the slope of the MDR is due primarily to changes in the high-density population fraction. A flattening of the f_{E+S0} – density relation with increasing redshift can be a consequence of environmentally-driven transformation of galaxies from late to early-types. Our new results provide direct measurements of the lenticular population fraction at $z \sim 1$ and we conclude that the observed differences in the morphology – density relation at $z \sim 1$ are due primarily to a deficit of S0 galaxies and an excess of Sp+Irr galaxies relative to the local galaxy population. The f_E – density relation does not appear to evolve over the range $0 < z < 1.3$. A deeper understanding of the implications of these results for models of galaxy and cluster formation will require further exploration of the dependence of morphological population fractions on galaxy mass and an assessment of the frequency of cluster galaxy merger activity.
3. The MDR at $z = 0.83$ is not sensitive to the rest-frame B -band luminosity for galaxies with luminosities brighter than $M^* + 1.2$ and in regions with $\Sigma > 30$ galaxies Mpc^{-2} . Work done at low redshift suggests, however, that luminosity effects may be more pronounced at fainter luminosities and in regions of lower density. Our present survey is not well-suited to studying these regimes.

4. We directly measure the lenticular population fraction and find $f_{S0} = 0.20 \pm 0.12$ when we average over densities with $\Sigma \geq 30$ galaxies Mpc^{-2} . The error in f_{S0} includes contributions from both counting statistics (± 0.035) and errors in our ability to visually classify lenticular galaxies (± 0.11). Our $z \sim 1$ f_{S0} value is about a factor of 2 less than the f_{S0} seen in similarly dense environments in the local universe but is comparable to what is seen at $0.4 \lesssim z \lesssim 0.5$. Our 20% population fraction of S0 galaxies is higher than almost all of the scenarios proposed by Smith et al. (2004) to explain the shallower f_{E+S0} – density relation – they predict $f_{S0} < 0.1$. However, a small reduction in the elliptical population fraction at $z = 0.5$ adopted by Smith et al. (2004) from $f_E = 0.6$ to $f_E = 0.5$, a value that appears to be in better agreement with the observations, is sufficient to increase their predicted $z = 1$ S0 population fractions to 0.2 ± 0.1 , overlapping our measurement. The distribution of ellipticities in $z > 0.8$ bulge-dominated (E+S0) cluster galaxies is inconsistent with an ellipticity distribution that would arise from a sample consisting solely of elliptical galaxies. In other words, our results suggest that rich clusters at $z \sim 1$ most likely have a significant population of lenticular galaxies and, therefore, a significant percentage of lenticular galaxies could have formed at redshifts $z > 1.3$.
5. We measure the morphology – radius relation and find its evolution is consistent with that seen in the morphology – density relation:
 - (a) the bulk of the transition from a f_{Sp+Irr} consistent with that in the field environment to its minimum value occurs within a radius of $0.6r_{200}$ (which corresponds, on average, to densities > 70 galaxies Mpc^{-2} and to physical scales less than ~ 750 kpc),
 - (b) the $z \sim 1$ f_{E+S0} value, at a given radius, is systematically less than the low- z f_{E+S0} for radii less than $\sim r_{200}$, and
 - (c) the f_{S0} – radius relation shows the most significant difference from the current epoch relationship.

However, elongation of and clumpiness in the galaxy distributions for many of our $z > 0.8$ clusters makes interpretation of the azimuthally-averaged morphology – radius relation more difficult (and perhaps less meaningful) than trends between morphology and local density.

6. We find that the bulge-dominated galaxy population fraction, f_{E+S0} , is mildly correlated with the bolometric X-ray luminosity of the cluster. Clusters with high X-ray luminosities have higher f_{E+S0} values within r_{200} than clusters with lower X-ray luminosities. In the present sample, the trend is significant at the $\lesssim 3\sigma$ level. A correlation between f_{E+S0} and bolometric X-ray luminosity can arise as a consequence either of environmentally-driven transformation processes or initial conditions. However, we do not find significant correlations between f_{E+S0} and the X-ray temperature

or cluster velocity dispersion. A definitive study of the relation between galaxy population fraction and cluster X-ray properties will require the analysis of large homogeneously selected cluster samples.

ACKNOWLEDGMENTS

ACS was developed under NASA contract NAS5-32865 and this research has been supported by NASA grant NAG5-7697. The STScI is operated by AURA Inc., under NASA contract NAS5-26555. We are grateful to Ken Anderson, Jon McCann, Sharon Busching, Alex Framarini, Sharon Barkhouser, and Terry Allen for their invaluable contributions to the ACS project at JHU. We wish to thank the referee, Alan Dressler, for his insightful comments.

TABLE 1
SUMMARY OF SPECTROSCOPIC AND HST OBSERVATIONS

Cluster	Redshift	N_z	$N_{z,CLACS}$	Mosaic Area (sq.arcmin)	Filter (Exp. Time in ksec)	HST ID
MS 1054–0321	0.831	327	143	35.5	V_{606} (2.0), i_{775} (4.0), z_{850} (4.0)	9290, 9919
RXJ 0152–1357	0.837	123	93	36.5	r_{625} (4.8), i_{775} (4.8), z_{850} (4.8)	9290
CL 1604+4304	0.900	107	20	12.0	V_{606} (4.8), I_{814} (4.8)	9919
CL 1604+4321	0.921	130	31	12.0	V_{606} (4.8), I_{814} (4.8)	9919
RDCS 0910+5422	1.101	~ 10	~ 10	12.2	i_{775} (6.8), z_{850} (11.4)	9919
RDCS 1252–2927	1.235	180	31	32.7	i_{775} (7.2), z_{850} (12.0)	9290
RXJ 0849+4452	1.266	90	16	33.7	i_{775} (7.3), z_{850} (12.2)	9919

TABLE 2
SUMMARY OF CLUSTER X-RAY AND KINEMATIC DATA

Cluster	L_x ($10^{44} h_{70}^{-2} \text{ erg s}^{-1}$)	$L_{x,\text{Bol}}$ ($10^{44} h_{70}^{-2} \text{ erg s}^{-1}$)	T_x (keV)	σ (km s^{-1})	r_{200} ($h_{70}^{-1} \text{ Mpc}$)	X-ray Data Reference	Vel. Disp. Reference
MS 1054–0321	7.78 ± 0.4	16.43 ± 0.8	$8.0^{+2.5}_{-1.5}$	1153 ± 80	1.79	1, 2	10
RXJ 0152–1357	5.74 ± 0.6	18.57 ± 1.9	$6.46^{+1.7}_{-1.2}$	919 ± 168	1.42	2, 3	11
CL 1604+4304	0.86 ± 0.13	2.01 ± 0.3	$2.51^{+1.05}_{-0.69}$	989^{+98}_{-76}	1.48	4	12
CL 1604+4321	< 0.7	649^{+59}_{-46}	0.95		12
RDCS 0910+5422	0.78 ± 0.09	2.14 ± 0.3	$7.20^{+2.2}_{-1.4}$...	0.99^a	5	
RDCS 1252–2927	1.90 ± 0.3	6.60 ± 1.1	6.50 ± 0.5	760^{+117}_{-69}	0.94	6, 7	13
RXJ 0849+4452	1.41 ± 0.3	2.85 ± 0.6	$5.80^{+2.8}_{-1.7}$...	0.91^a	8, 9	

^a r_{200} based on assumed $\sigma = 750 \text{ km s}^{-1}$

¹Gioia et al. 2004; Donahue 2004, priv. comm.

²Romer et al. 2000

³Della Ceca et al. 2000

⁴Lubin et al. 2004

⁵Stanford et al. 2002

⁶Rosati et al. 2004

⁷Lombardi et al. 2005

⁸Rosati et al. 1999

⁹Stanford et al. 2001

¹⁰Gioia et al. 2004

¹¹Demarco et al. 2004

¹²Gal & Lubin 2004

¹³Demarco et al. 2004a

TABLE 3
POPULATION FRACTIONS AS A FUNCTION OF PROJECTED DENSITY

Cluster or Sample	$N(\Sigma)$	$\log_{10}(\Sigma)$ (Gals Mpc $^{-2}$)	f_{E+S0}	f_E	f_{S0}	f_{Sp+Irr}
$z \sim 1$ composite	136	1.30	0.45 ± 0.11	0.32 ± 0.14	0.13 ± 0.14	0.56 ± 0.11
	220	1.60	0.35 ± 0.09	0.22 ± 0.13	0.13 ± 0.13	0.65 ± 0.09
	237	1.90	0.53 ± 0.09	0.31 ± 0.13	0.22 ± 0.13	0.47 ± 0.09
	138	2.20	0.62 ± 0.10	0.39 ± 0.14	0.23 ± 0.14	0.38 ± 0.10
	87	2.50	0.71 ± 0.12	0.47 ± 0.15	0.24 ± 0.15	0.29 ± 0.12
	24	2.80	0.65 ± 0.21	0.53 ± 0.23	0.12 ± 0.23	0.35 ± 0.21
	14	3.10	0.87 ± 0.27	0.71 ± 0.29	0.16 ± 0.29	0.12 ± 0.27
$z \sim 1$ composite	185	1.06 ± 0.2	0.30 ± 0.10	0.24 ± 0.13	0.06 ± 0.13	0.70 ± 0.10
	595	2.06 ± 0.2	0.51 ± 0.07	0.31 ± 0.12	0.20 ± 0.12	0.49 ± 0.07
	38	3.06 ± 0.2	0.73 ± 0.17	0.59 ± 0.20	0.14 ± 0.20	0.27 ± 0.17
$z < 0.6$ composite	435	2.06 ± 0.2	0.63 ± 0.08	0.34 ± 0.12	0.29 ± 0.12	0.37 ± 0.08
	66	3.06 ± 0.2	0.80 ± 0.14	0.50 ± 0.17	0.30 ± 0.17	0.20 ± 0.14
MS 1054–0321	79	≥ 2.00	0.80 ± 0.13	0.49 ± 0.16	0.31 ± 0.16	0.20 ± 0.13
RXJ 0152–1357	63	≥ 2.00	0.81 ± 0.14	0.56 ± 0.17	0.25 ± 0.17	0.20 ± 0.14
CL 1604+4304	62	≥ 2.00	0.53 ± 0.14	0.33 ± 0.17	0.20 ± 0.17	0.47 ± 0.14
CL 1604+4321	86	≥ 2.00	0.39 ± 0.12	0.25 ± 0.15	0.14 ± 0.15	0.61 ± 0.12
RDCS 0910+5422	43	≥ 2.00	0.50 ± 0.16	0.37 ± 0.19	0.13 ± 0.19	0.50 ± 0.16
RDCS 1252–2927	46	≥ 2.00	0.85 ± 0.16	0.62 ± 0.18	0.23 ± 0.18	0.15 ± 0.16
RXJ 0849+4452	104	≥ 2.00	0.35 ± 0.11	0.33 ± 0.14	0.02 ± 0.14	0.65 ± 0.11

Errors are the quadrature sum of counting statistics and classification uncertainty. See text for details.

TABLE 4
POPULATION FRACTIONS AS A FUNCTION OF R_{200} RADIUS

Cluster or Sample	$N(r/R_{200})$	r/R_{200}	f_{E+S0}	f_E	f_{S0}	f_{Sp+Irr}
$z \sim 1$ composite	63	0.05	0.75 ± 0.14	0.52 ± 0.17	0.23 ± 0.17	0.26 ± 0.14
	80	0.15	0.52 ± 0.13	0.37 ± 0.16	0.15 ± 0.16	0.48 ± 0.13
	90	0.25	0.56 ± 0.12	0.35 ± 0.15	0.21 ± 0.15	0.44 ± 0.12
	83	0.35	0.45 ± 0.13	0.24 ± 0.16	0.21 ± 0.16	0.55 ± 0.13
	94	0.45	0.42 ± 0.12	0.25 ± 0.15	0.17 ± 0.15	0.58 ± 0.12
	99	0.55	0.27 ± 0.12	0.21 ± 0.15	0.06 ± 0.15	0.73 ± 0.12
	114	0.65	0.32 ± 0.11	0.20 ± 0.15	0.12 ± 0.15	0.69 ± 0.11
	129	0.75	0.30 ± 0.11	0.15 ± 0.14	0.15 ± 0.14	0.70 ± 0.11
	96	0.85	0.35 ± 0.12	0.11 ± 0.15	0.24 ± 0.15	0.64 ± 0.12
	74	0.95	0.25 ± 0.13	0.15 ± 0.16	0.10 ± 0.16	0.75 ± 0.13
	23	1.05	0.32 ± 0.22	0.32 ± 0.24	0.00 ± 0.24	0.68 ± 0.22
11	1.15	0.19 ± 0.31	0.00 ± 0.32	0.19 ± 0.32	0.81 ± 0.31	
MS 1054–0321	130	≤ 1.0	0.78 ± 0.11	0.46 ± 0.14	0.32 ± 0.14	0.22 ± 0.11
RXJ 0152–1357	125	≤ 1.0	0.72 ± 0.11	0.46 ± 0.14	0.26 ± 0.14	0.27 ± 0.11
CL 1604+4304	124	≤ 1.0	0.57 ± 0.11	0.40 ± 0.14	0.17 ± 0.14	0.42 ± 0.11
CL 1604+4321	150	≤ 1.0	0.39 ± 0.10	0.27 ± 0.14	0.12 ± 0.14	0.60 ± 0.10
RDCS 0910+5422	146	≤ 1.0	0.38 ± 0.10	0.32 ± 0.14	0.06 ± 0.14	0.61 ± 0.10
RDCS 1252–2927	67	≤ 1.0	0.68 ± 0.14	0.47 ± 0.16	0.21 ± 0.16	0.32 ± 0.14
RXJ 0848+4452	214	≤ 1.0	0.30 ± 0.09	0.29 ± 0.13	0.01 ± 0.13	0.70 ± 0.09

Errors are the quadrature sum of counting statistics and classification uncertainty. See text for details.

APPENDIX

COMPARING PROJECTED DENSITY ESTIMATION TECHNIQUES

We demonstrate here that the Nearest Neighbor (NN) and Friends-of-Friends (FoF) algorithms for estimating local projected density yield consistent results. We also show that it is possible to construct a composite MDR or MRR using a combination of galaxy samples selected using spectroscopic redshifts, photometric redshifts, and samples with only statistically subtracted background corrections providing each of the samples are confined to specific density ranges.

The FoF algorithm provides an alternative to the NN algorithm as a means to measure the morphological composition as a function of density. The FoF algorithm, first developed by Huchra & Geller (1982), has been used widely thereafter for automated detection of overdensities in galaxy catalogs. This approach has the advantage that it is not tied to a specific choice of N nearest neighbors although it is not the method typically used by other workers in the analysis of the MDR. The FoF algorithm locates groups of galaxies by identifying all the neighboring systems that lie within a given “percolation” length of a given galaxy. Each neighbor is then searched for galaxies within the same percolation length. This linking process is continued until no additional members can be identified. The percolation length and the local projected density are related as $l_{perc} \propto 1/\sqrt{\Sigma}$. For our comparison, we use percolation lengths that correspond to overdensities in the range $15 < \Sigma < 1500$ galaxies Mpc^{-2} . At each overdensity, the morphological populations within all identified groups are tallied, weighted by the inverse of the selection function. The difference between the cumulative E, S0, and Sp+Irr population at two overdensities Σ and $\Sigma - \delta\Sigma$ then defines the morphological populations at projected density Σ . As with the nearest neighbor algorithm, we correct the FoF densities to correspond to our fiducial luminosity limit using equation 2.

Figure A16 shows a comparison between the NN and FoF density estimators for the clusters for which we have reliable photometric redshifts (MS1054-0321, RXJ0152-1357, and RDCS1252-2927). The errorbars in all these figures include the uncertainties from counting statistics and from the intrinsic classification uncertainties quantified in section 3 (*e.g.*, ± 0.06 in f_{E+S0} and f_{Sp+Irr} ; ± 0.11 in f_{S0} and f_E). The two density estimators produce consistent results over the full range of densities analyzed.

Using Composite Cluster Samples

Because not all clusters in our sample have sufficient data to compute the local density based on either spectroscopic or on photometric redshift values, it is also important to establish that our results are not very sensitive to the details used to derive the MDR (*e.g.*, whether the sample is selected based on photometric redshift value, spectroscopic redshift value, or a flux-limited sample with statistical background subtraction). If we can demonstrate this then we can construct a composite MDR by combining for each individual cluster the sample that yields the most reliable available estimate (*e.g.*, the samples with the least contamination from foreground/background objects). The clusters

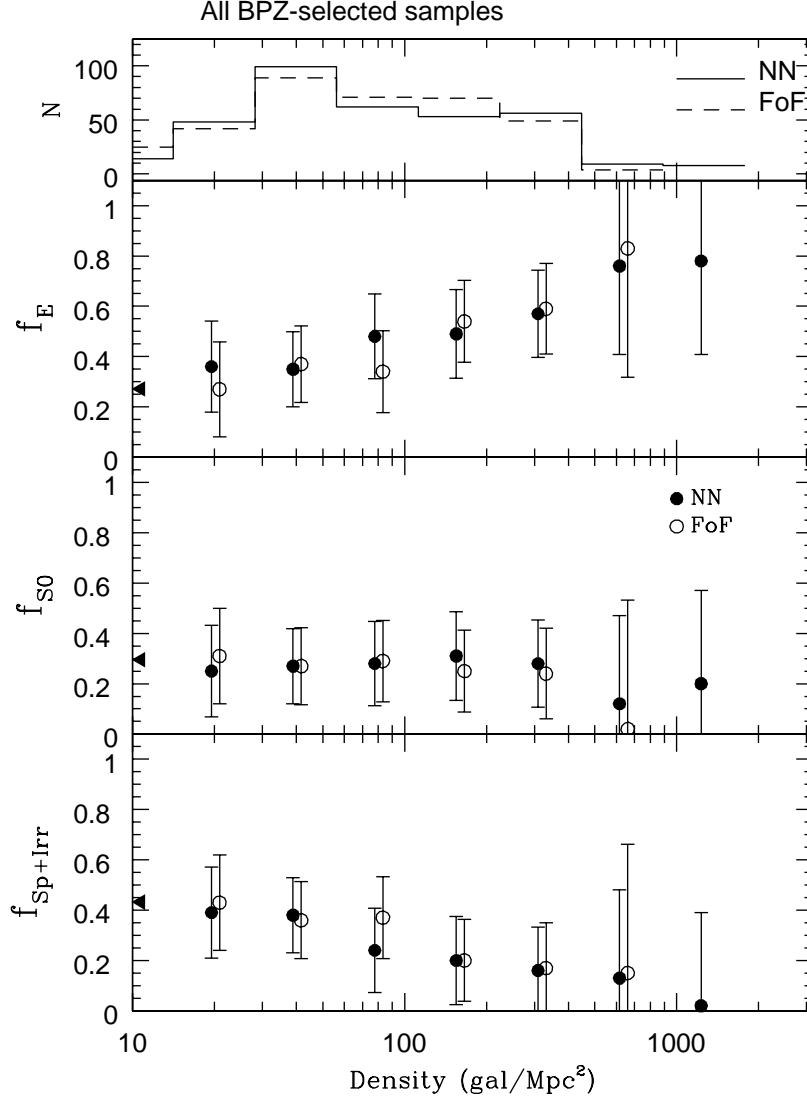


FIG. A16.— The composite morphology – density relation for the clusters MS1054-0321, RXJ0152-1357, and RDCS1252-2927. These results are based on the photo- z selected samples that include galaxies with z_{ph} values in the range $|\bar{z}_{cl} - z_{ph}|/(1 + z_{cl}) \leq 2\sigma_{ph}$. Results from the N th nearest-neighbor (NN) and friends-of-friends (FoF) density estimators are both shown here. The density values have been offset by a small amount from one another for clarity. The total number of galaxies in each density bin is shown in the top panel of the plot. The low-density population fractions from the SDSS (Goto et al. 2003a) are denoted by the triangles along the y-axis.

RXJ0152-1357 and MS1054-0321 allow us to perform this test as they have sufficient information to independently generate the MDR from spectroscopic data, from photometric redshift data, and from flux-limited samples with a statistically-subtracted background correction applied. The results are shown in Figure A17. For densities greater than 80 galaxies Mpc^{-2} there are no significant systematic differences in any of the derived population fractions as a function of density. Below 80 galaxies Mpc^{-2} , the statistically subtracted background corrected density and population fraction estimates become less reliable as fluctuations in the background galaxy surface density become comparable with the projected density (see discussion in section 4). The spectroscopic samples exhibit a lower elliptical galaxy fraction at densities below about 50 galaxies Mpc^{-2} but the differences lie within the 1σ uncertainties. The spectroscopic data do not provide good sampling of the very highest densities ($\Sigma > 1000$ galaxies Mpc^{-2}) because of the number of slit masks used. However, in this regime, the photo- z and/or statistically subtracted background results are very reliable. We conclude that the MDR and MRR derived from a composite sample will be reliable if spectroscopically selected samples are limited to regions with $\Sigma \leq 1000$ galaxies Mpc^{-2} and samples with statistically subtracted background corrections are limited to regions with $\Sigma > 80$ galaxies Mpc^{-2} .

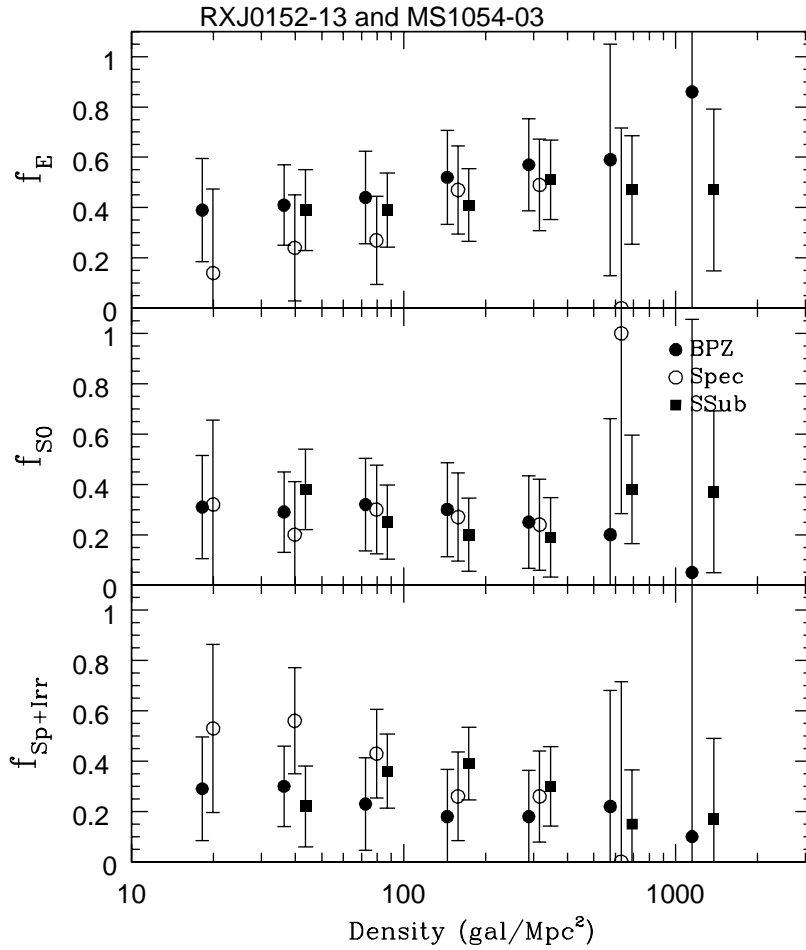


FIG. A17.— The dependence of MDR on sample selection is demonstrated for MS1054-0321 and RXJ0152-1357. We show the population fractions as a function of projected density based on the samples of confirmed spectroscopic members (Spec), the samples of photo-z selected members (BPZ), and on the full flux-limited samples with statistically subtracted background corrections applied (SSub). The latter results are only shown when $\Sigma > 40$ galaxies Mpc^{-2} . Errorbars include the uncertainties in counting statistics and morphological classification.

COMPUTING MORPHOLOGICAL POPULATION FRACTIONS

Our morphological population fractions are corrected for both contamination and incompleteness in a manner that depends on the sample being analyzed. For samples using only confirmed spectroscopic redshifts, the only correction applied is the weighting by the inverse of the redshift selection function (cf. equation 1). The redshift selection function is computed empirically by measuring the ratio of the number of redshifts acquired to the total number of galaxies in magnitude bins 0.5 mag wide. The redshift selection function is dependent on the galaxy magnitude and to a lesser degree on the galaxy color. The latter dependence translates to a dependence on morphology for those galaxies in the cluster. By measuring the redshift completeness as a function of color and magnitude, we can make reasonable corrections for the observational selection effects. The clusters for which we have a sufficient number of redshifts to compute the MDR solely from a spectroscopic sample are MS1054-0321 (with 143 confirmed members, all within the boundaries of our ACS mosaic) and RXJ0152-1357 (with 102 confirmed members, 93 of which lie within the boundaries of our ACS mosaic). The redshift selection functions for these two clusters is shown as a function of i_{775} magnitude and morphological type in Figure B18.

For photometric redshift selected samples (MS1054-0321, RXJ0152-1357, and RDCS1252-2927), we correct the population fractions as follows:

$$N_T^{corr} = N_T^{uncorr} + N_T^{missed} - N_T^{contam} \quad (\text{B1})$$

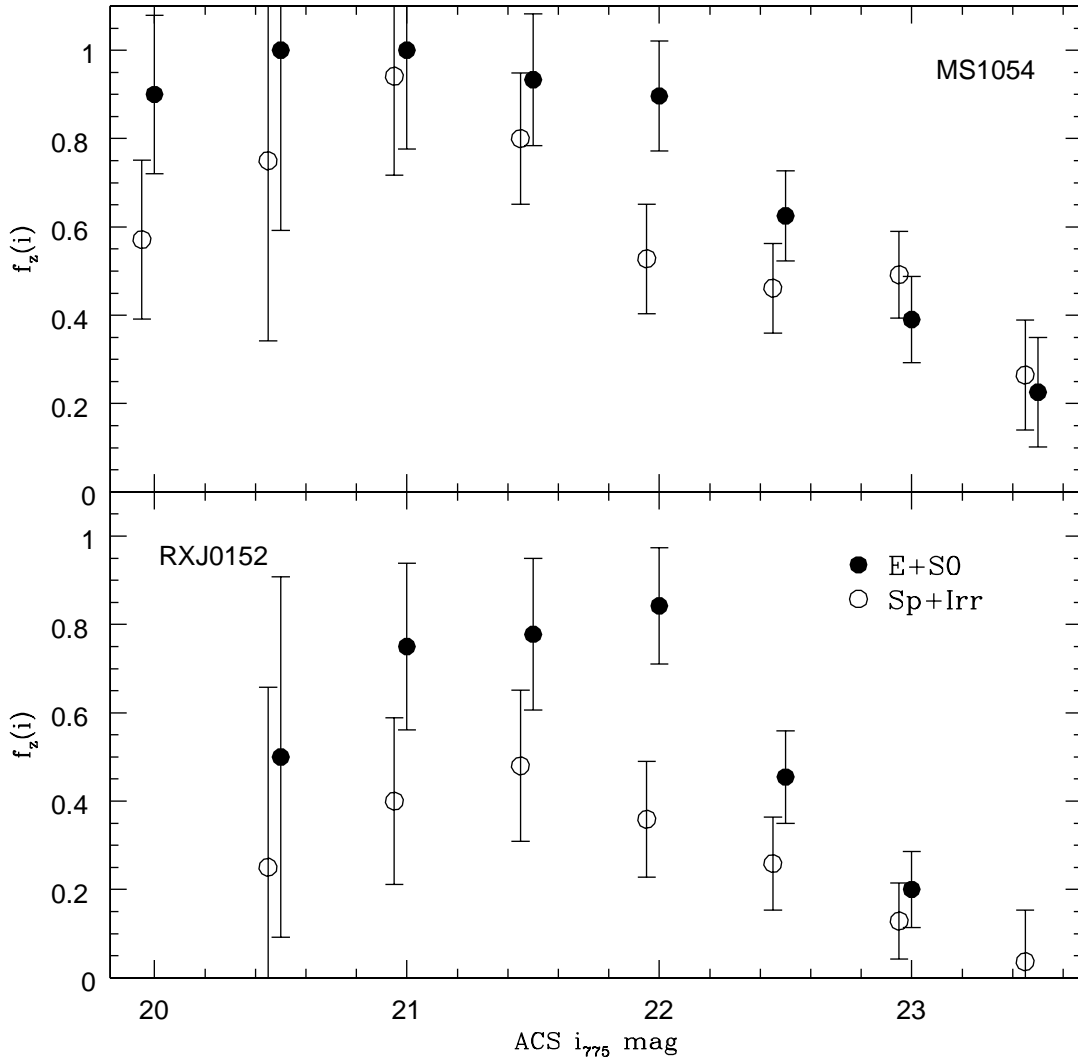


FIG. B18.— The redshift selection functions for E+S0 and Sp+Irr galaxies vs. i_{775} magnitude for MS1054-0321 and RXJ0152-1357. The larger difference between E+S0 and Sp+Irr selection efficiency in RXJ0152-1357 is caused by the color selection criterion used in target selection for that cluster.

where N_T^{uncor} is the observed number of galaxies of morphological type T , N_T^{missed} is an estimate of the number of cluster members of type T that have been excluded by our photo- z selection criteria, and N_T^{contam} is an estimate of the number of non-cluster members of type T that have been included in the observed count. The number of missed members is computed as follows:

$$N_T^{missed} = N_{total} \times f_{tot,miss} \times f_{miss,T} \quad (\text{B2})$$

where N_{total} is the total number of galaxies counted at a given density, $f_{tot,miss}$ is the fraction of cluster members excluded by our photo- z selection limits, and $f_{miss,T}$ is the fraction of those excluded galaxies that have morphological type T . The value of $f_{tot,miss}$ is estimated by counting the number of spectroscopically confirmed members that have photo- z 's outside our photo- z selection limits. For MS1054-0321 and RXJ0152-1357, $f_{tot,miss} = 0.38$ and 0.20 , respectively. For RDCS1252-2927, $f_{tot,miss} = 0.04$. The morphological dependence of the number of true cluster galaxies missed by our photo- z selection is weak for MS1054-0321 and RDCS1252-2927 but is more significant for RXJ0152-1357 (see Figure B18). For MS1054-0321 and RDCS1252-2927, we set $f_{miss,T}$ equal to the initial uncorrected population fraction for galaxies of type T at the given density. For RXJ0152-1357 we assign $f_{miss,T}$ using a morphological distribution that is slightly more heavily weighted to late-type galaxies at a given density to compensate for the spectroscopic selection bias in this cluster. Fortunately, the results are not strongly dependent on the precise prescriptions for setting the $f_{miss,T}$ values. The number of non-cluster members contaminating our photo- z selected counts is computed as follows:

$$N_T^{contam} = N_{total} \times f_{tot,contam} \times f_{contam,T} \quad (\text{B3})$$

where $f_{tot,contam}$ is the fraction of non-cluster members included by our photo- z selection limits and $f_{contam,T}$ is the fraction of these that have morphological type T . The value of $f_{tot,contam}$ is estimated by counting the number of spectroscopically confirmed non-cluster members that have photo- z 's lying within our photo- z selection limits. For MS1054-0321 and RXJ0152-1357, $f_{tot,contam} = 0.09$ and 0.12 , respectively. For RDCS1252-2927, $f_{tot,contam} = 0.33$. These non-cluster galaxies have a morphological distribution that is representative of the field galaxy population and we thus set $f_{contam,E} = 0.10$, $f_{contam,S0} = 0.25$, and $f_{contam,Sp+Irr} = 0.65$. Note that because we only have ~ 35 spectroscopic redshifts for RDCS1252-2927, the incompleteness and contamination estimates have larger uncertainties than those in MS1054-0321 or RXJ0152-1357.

For population fractions derived from magnitude limited samples using only statistically-subtracted background counts (*e.g.*, as in RDCS0910+5422), the morphological distribution of the background is assumed to be representative of the field galaxy population and we thus divide the expected background counts into E, S0, and Sp+Irr components assuming the same fractions given above: $f_E = 0.10$, $f_{S0} = 0.25$, and $f_{Sp+Irr} = 0.65$.

REFERENCES

- Abadi, M. G., Moore, B., Bower, R. G. 1999, MNRAS, 308, 947
 Abraham, R. G., Valdes, F., Yee, H. K. C., & van den Bergh, S. 1994, ApJ, 432, 75
 Abraham, R. G. & van den Bergh, S. 2001, Science, 293, 1273
 Bartko, F. et al. 2005, in preparation.
 Bekki, K. 1998, ApJ, 502, 133
 Bekki, K., Couch, W. J., Shioya, Y. 2002, ApJ, 577, 651
 Benítez, N. 2000, ApJ, 536, 57
 Benítez, N., et al. 2004, ApJS, 150, 1
 Benson, A. J., Frenk, C. S., Baugh, C. M., Cole, S., Lacey, C. G. 2001, MNRAS, 327, 1041
 Bertin, E. & Arnouts, S. 1996, A&AS, 117, 393
 Blakeslee, J. P., Anderson, K. R., Meurer, G. R., Benítez, N., & Magee, D. 2003a, ASP Conf. Ser. 295: Astronomical Data Analysis Software and Systems XII, 12, 257
 Blakeslee, J. P., et al. 2003b, ApJ, 596, L143
 Bouwens, R., Broadhurst, T., & Silk, J. 1998, ApJ, 506, 557
 Bunker, A., Spinrad, H., Stern, D., Thompson, R., Moustakas, L., Davis, M., Dey, A. 2000, astro-ph/0004348
 Byrd, G., & Valtonen, M. 1990, ApJ, 350, 89
 Carlberg, R. G., Yee, H. K. C., & Ellingson, E. 1997, ApJ, 478, 462
 Conselice, C. J., Bershady, M. A., & Jangren, A. 2000, ApJ, 529, 886
 De Propris, R., et al. 2004, MNRAS, 351, 125
 Della Ceca, R., Scaramella, R., Gioia, I. M., Rosati, P., Fiore, F., & Squires, G. 2000, A&A, 353, 498
 Demarco, R., Rosati, P., et al. 2004, A&A, submitted
 Demarco, R., Rosati, P., Lidman, C., Nonino, M., Mainieri, V., Stanford, A., Holden, B., & Eisenhardt, P. 2004a, *Carnegie Observatories Astrophysics Series, Vol 3: Clusters of Galaxies: Probes of Cosmological Structure and Galaxy Evolution*, eds. J. Mulchaey, A. Dressler, and A. Oemler.
 Demarco, R. et al. 2005, in preparation
 Donahue, M., Voit, G. M., Gioia, I., Lupino, G., Hughes, J. P., & Stocke, J. T. 1998, ApJ, 502, 550
 Dressler, A. 1980, ApJ, 236, 351 [D80]
 Dressler, A. et al. 1997, ApJ, 490, 577 [D97]
 Ettori, S., et al. 2004, MNRAS, 322, in press
 Fabricant, D., Franx, M., van Dokkum, P. 2000, ApJ, 539, 577
 Fairley, B. W., Jones, L. R., Wake, D. A., Collins, C. A., Burke, D. J., Nichol, R. C., & Romer, A. K. 2002, MNRAS, 330, 755
 Farouki, R., & Shapiro, S. L. 1980, ApJ, 241, 928
 Fasano, G., Poggianti, B. M., Couch, W. J., Bettoni, D., Kjærgaard, P., & Moles, M. 2000, ApJ, 542, 673
 Ferguson, H. C., et al. 2004, ApJ, 600, 107
 Finn, R. A., Zaritsky, D., & McCarthy, D. W. 2004, ApJ, 604, 141
 Ford, H. C., Clampin, M., et al. 2003, Proc. SPIE, 4854, 81
 Fujita, Y. 1998, ApJ, 509, 587
 Fujita, Y., & Nagashima, M. 1999, ApJ, 516, 619
 Gal, R. R. & Lubin, L. M. 2004, ApJ, 607, L1
 Gioia, I. M., Braito, V., Branchesi, M., Della Ceca, R., Maccacaro, T., & Tran, K.-V. 2004, A&A, 419, 517
 Goto, T., Yamauchi, C., Fujita, Y., Okamura, S., Sekiguchi, M., Smail, I., Bernardi, M., Gomez, P. 2003a, MNRAS, 346, 601
 Goto, T., et al. 2003b, PASJ, 55, 739
 Goto, T., Yagi, M., Tanaka, M., & Okamura, S. 2004, MNRAS, 348, 515
 Goto, T., et al. 2004, ApJ, submitted
 Gunn, J. E., & Gott, R. 1972, ApJ, 176, 1
 Heavens, A., Panter, B., Jimenez, R., Dunlop, J. 2004, Nature, 428, 625
 Homeier, N., et al. 2005, ApJ, in press
 Huchra, J. P., & Geller, M. J. 1982, ApJ, 257, 423
 Icke, V. 1985, A&A, 144, 115
 Kauffmann, G. 1995, MNRAS, 274, 161
 Kent, S. M. 1981, ApJ, 245, 805
 Kodama, T., Smail, I., Nakata, F., Okamura, S., & Bower, R. G. 2001, ApJ, 562, L9
 Kodama, T. & Smail, I. 2001, MNRAS, 326, 637
 Larson, R. B., Tinsley, B. M., Caldwell, C. N. 1980, ApJ, 237, 692
 Lavery, R. J., & Henry, J. P. 1988, ApJ, 330, 596
 Lombardi, M., Rosati, P., Blakeslee, J. P., Ettori, S., Demarco, R., Ford, H. C., Illingworth, G. D., Clampin, M., Hartig, G. F., Benítez, N., Broadhurst, T. J., Franx, M., Jee, M. J., Postman, M., & White, R. L. 2005, ApJ, in press.
 Lubin, L. M., Mulchaey, J. S., & Postman, M. 2004, ApJ, 601, L9
 Makino, J., & Hut, P. 1997, ApJ, 481, 83
 Mamon, G. A. 1992, ApJ, 401, L3
 Margoniner, V. E., de Carvalho, R. R., Gal, R. R., & Djorgovski, S. G. 2001, ApJ, 548, L143
 Moore, B., Katz, N., Lake, G., Dressler, A., Oemler, A. 1996, Nature, 379, 613
 Moore, B., Lake, G., Quinn, T., Stadel, J. 1999, MNRAS, 304, 465
 Moss, C. & Whittle, M. 2000, MNRAS, 317, 667
 Mulchaey, J., & Zabludoff, A. I. 1998, ApJ, 496, 73
 Okamoto, T. & Nagashima, M. 2003, ApJ, 587, 500
 Papovich, C., Giavalisco, M., Dickinson, M., Conselice, C. J., & Ferguson, H. C. 2003, ApJ, 598, 827
 Poggianti, B. M., Smail, I., Dressler, A., Couch, W. J., Barger, A. J., Butcher, H., Ellis, R. S., & Oemler, A. J. 1999, ApJ, 518, 576
 Ponman, T. J., Bourner, P. D. J., Ebeling, H., Bohringer, H. 1996, MNRAS, 283, 601
 Postman, M. & Geller, M. J., 1984, ApJ, 281, 95 [PG84]
 Postman, M., Lubin, L. M., Oke, J. B. 1998a, AJ, 116, 560
 Postman, M., Lauer, T. R., Szapudi, I., Oegerle, W. 1998b, ApJ, 506, 33
 Postman, M., Lubin, L., Oke, J. B. 2001, AJ, 122, 1125
 Quilis, V., Moore, B., Bower, R. 2000, Science, 288, 1617
 Roche, N., Ratnatunga, K., Griffiths, R. E., Im, M., & Naim, A. 1998, MNRAS, 293, 157
 Romer, A. K., et al. 2000, ApJS, 126, 209
 Rosati, P., Stanford, S. A., Eisenhardt, P. R., Elston, R., Spinrad, H., Stern, D., & Dey, A. 1999, AJ, 118, 76
 Rosati, P., et al. 2004, AJ, 127, 230
 Schlegel, D. J., Finkbeiner, D. P., Davis, M. 1998, ApJS, 500, 525
 Smith, G. P., Treu, T., Ellis, R. S., Moran, S. M., Dressler, A. 2004, astro-ph/0403455, ApJ, submitted [Sm04]
 Stanford, S. A., Elston, R., Eisenhardt, P., Spinrad, H., Stern, D., Dey, A. 1997, AJ, 114, 2232
 Stanford, S. A., Holden, B., Rosati, P., Tozzi, P., Borgani, S., Eisenhardt, P. R., & Spinrad, H. 2001, ApJ, 552, 504
 Stanford, S. A., Holden, B., Rosati, P., Eisenhardt, P. R., Stern, D., Squires, G., & Spinrad, H. 2002, AJ, 123, 619
 Tanaka, M., Goto, T., Okamura, S., Shimasaku, K., Brinkman, J., 2005, AJ, in press.
 Toft, S., Mainieri, V., Rosati, P., Lidman, C., Demarco, R., Nonino, M., & Stanford, S. A. 2004, A&A, 422, 29

- Tran, K., Magee, D., Franx, M., Illingworth, G. D., Kelson, D., van Dokkum, P. 2005, in preparation.
- Treu, T., Ellis, R. S., Kneib, J., Dressler, A., Smail, I., Czoske, O., Oemler, A., & Natarajan, P. 2003, *ApJ*, 591, 53
- Trujillo, I., et al. 2004, *ApJ*, 604, 521
- Tully, R. B. & Shaya, E. J. 1984, *ApJ*, 281, 31
- Valluri, M. 1993, *ApJ*, 408, 57
- van Dokkum, P. G., Franx, M., Fabricant, D., Illingworth, G. D., Kelson, D. D. 2000, *ApJ*, 541, 95
- Whitmore, B. C., & Gilmore, D. M. 1991, *ApJ*, 367, 64
- Windhorst, R., et al. 2002, *ApJS*, 143, 113
- Xue, Y. & Wu, X. 2000, *ApJ*, 538, 65
- Zabludoff, A. I., & Mulchaey, J. S. 1998, *ApJ*, 496, 39

This figure "f2.jpg" is available in "jpg" format from:

<http://arxiv.org/ps/astro-ph/0501224v2>

This figure "f3.jpg" is available in "jpg" format from:

<http://arxiv.org/ps/astro-ph/0501224v2>

This figure "f6.jpg" is available in "jpg" format from:

<http://arxiv.org/ps/astro-ph/0501224v2>

This figure "f8.jpg" is available in "jpg" format from:

<http://arxiv.org/ps/astro-ph/0501224v2>